



# 1 Introduction

The production of pairs of direct photons<sup>1</sup> with large invariant mass is the so called irreducible background for the search of the Higgs boson in the two photon decay channel in the intermediate mass range  $80 \text{ GeV} < m_{\gamma\gamma} < 140 \text{ GeV}$  at the forthcoming LHC. This background is huge and requires to be understood and quantitatively evaluated.

Beside this important motivation, this process deserves interest by its own. The production of such pairs of photons has been experimentally studied in a large domain of energies, from fixed targets [1, 2, 3] to colliders [4, 5, 6]. A wide variety of observables has been measured, such as distributions of invariant mass, azimuthal angle and transverse momentum of the pairs of photons, inclusive transverse momentum distributions of each photon, which offer the opportunity to test our understanding of this process.

The aim of this article is to present a study of diphoton hadroproduction based on a computer code of partonic event generator type. In this code, we account for all contributing processes consistently at next-to-leading order (NLO) accuracy, together with the so called box contribution  $gg \rightarrow \gamma\gamma$ . This code is flexible enough to accommodate various kinematic or calorimetric cuts. Especially, it allows to compute cross sections for both inclusive and isolated direct photon pairs, for any infrared and collinear safe isolation criterion which can be implemented at the partonic level. This article is organized according to the following outline. In section 2, we remind the basic theoretical ingredients, and present the method used to build the computer code developed for this study. Section 3 is dedicated to the phenomenology of photon pair production. We start with a comparison with fixed target and collider experiments. We then provide some predictions for LHC, together with a discussion of theoretical scale uncertainties. The theoretical discussion about the present day limitations of our code is continued in section 4. There we mention various infrared sensitive situations, which would deserve some more care, and for which the resummation of multiple soft gluon effects would be required, in order to improve the ability of our code to account for such observables. Section 5 gathers our conclusions and perspectives.

## 2 Theoretical content and presentation of the method

Let us first remind briefly the theoretical level of accuracy and limitations of works prior to the present one, in order to assess the improvements which we introduce. Then we present the method which we used to build our computer code `DIPHONX`.

### 2.1 Theoretical content

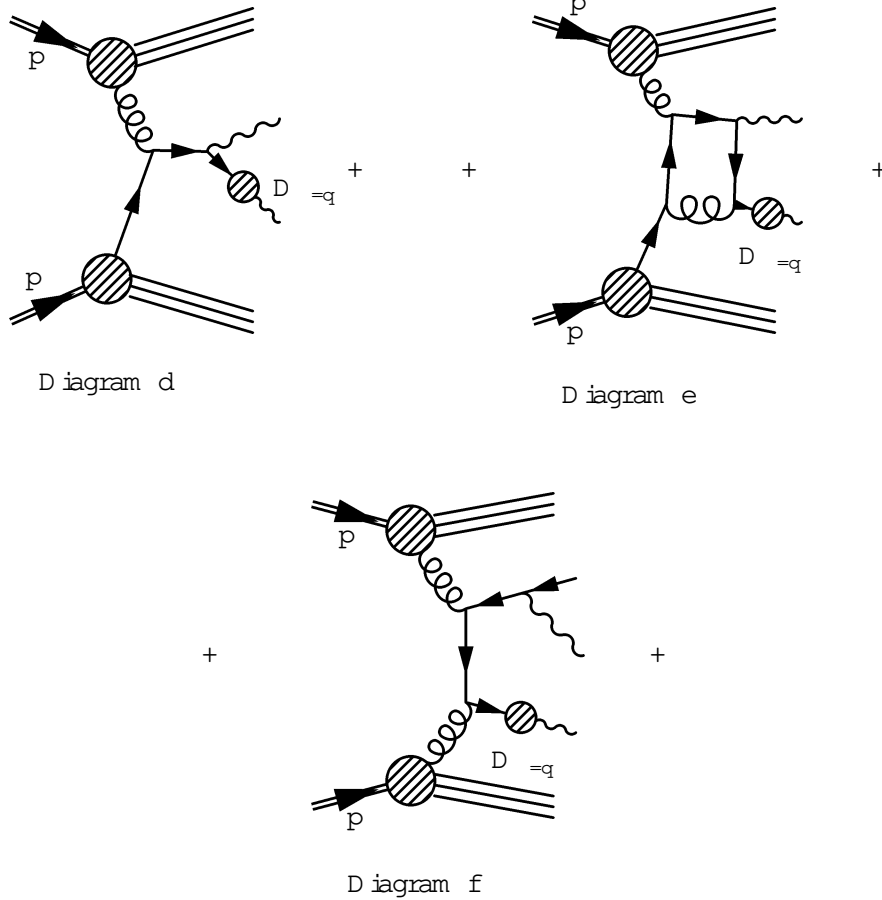
The theoretical understanding of this process relies on NLO calculations, initiated in [7]. The leading order contribution to diphoton reactions is given by the Born level process  $q\bar{q} \rightarrow \gamma\gamma$  (see for instance Diagram a). The computation of NLO contributions to it yields  $\mathcal{O}(\alpha_s)$  corrections coming from the subprocesses  $q\bar{q} \rightarrow g, gq$  (or  $q\bar{q} \rightarrow q$ ) and corresponding virtual corrections, see

---

<sup>1</sup>The word "direct" means here that these photons do not result from the decay of  $0, \rho, \omega, \dots$  at large transverse momentum. Direct photons may be produced according to two possible mechanisms: either they take part directly to the hard subprocess, or they result from the fragmentation of partons themselves produced at high transverse momentum in the subprocess; see sect. 2.



range 80 GeV  $m$  140 GeV. A consistent treatment of diphoton production at NLO thus requires that  $O(\alpha_s)$  corrections to these contributions be calculated also, see for example Diagrams e and f. They have not been incorporated in [7, 8, 9], and we compute them in the present work.



The calculation of these corrections in their turn yields the leading order contribution of yet another mechanism, of double fragmentation type, see for example Diagram g. In the latter case, both photons result from the collinear fragmentation of a hard parton. In order to present a study of consistent NLO accuracy, NLO corrections to this double fragmentation contribution, see for example Diagrams h and i, have to be calculated accordingly. This is also done in the present article.



one of the first motivations of the present work. Thus, even though it may be suggestive to compare the respective sizes and shapes of the separate contributions for a given choice of scale, as will be done in 3.2.1, we emphasize that only their sum is meaningful.

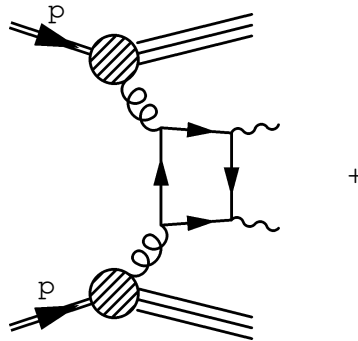


Diagram j

Beyond this, the  $O(\frac{2}{s})$  so-called box contribution  $gg \rightarrow gg$  through a quark loop is also included, see for example Diagram j. Strictly speaking it is a NNLO contribution from the point of view of power counting. However in the range of interest at LHC for the search of the Higgs boson, the gluon luminosity is so large compared with the quark and antiquark one, that it nearly compensates the extra powers of  $s$ , so as to yield a contribution comparable with the Born term. For this reason, it has been included in previous works, and will be in the present one as well. We define the "direct" contribution as the sum "two direct" + box.

Actually one should notice, first, that other NNLO gluon-gluon initiated processes, such as the collinear finite part of  $gg \rightarrow qq$  have been ignored<sup>3</sup>, although they could also be large. Secondly one should also even worry about the next correction to the box, because the latter may be quite sizeable. Such a possibility is suggested by the situation occurring to the first correction to the effective vertex  $gg \rightarrow h$ , computed in [11], and shown to reach generically about 50 % of the one-loop result. Moreover, this box contribution is the leading order of a new mechanism, whose spurious (factorization and renormalization) scale dependences are monotonic, and only higher order corrections would partly cure this problem and provide a quantitative estimate. This tremendous effort has not been carried out yet, although progresses towards this goal have been achieved recently [12, 13, 14].

## 2.2 Presentation of the method

In [7], a dedicated calculation was required for each observable. Since then more versatile approaches have been developed, which combine analytical and Monte-Carlo integration techniques [8], [15]. They thus allow the computation of several observables within the same calculation, at NLO accuracy, together with the incorporation of selection/isolation cuts at the partonic level in

<sup>3</sup>The collinear divergent parts of these 2 ! 4 processes have been already taken into account in the NLO corrections to the "one fragmentation" contribution and leading order "two fragmentation" components respectively.

order to match the various cuts used by the experimental collaborations as faithfully as possible. The studies of [8] and of [9] rely on such an approach. Let us briefly describe the one which we use here.

### 2.2.1 Phase space slicing and subtraction of long distance singularities

Within the combined analytical and Monte-Carlo approach, two generic well known methods can be used to deal with infrared and collinear singularities which are met in the calculation of inclusive cross sections: the phase space slicing method [16] and the subtraction method [17]. The approach followed in the present work uses a modified version of the one presented in [15], which combines these two techniques.

For a generic reaction  $1 + 2 \rightarrow 3 + 4 + 5$  two particles of the final state, say 3 and 4, have a high  $p_T$  and are well separated in phase space, while the last one, say 5, can be soft, or collinear to either of the four others. The phase space is sliced using two arbitrary, unphysical parameters  $p_{Tm}$  and  $R$  in the following way:

- Part I

The norm  $p_{T5}$  of transverse momentum of the particle 5 is required to be less than some arbitrary value  $p_{Tm}$  taken to be small compared to the other transverse momenta. This cylinder supplies the infrared, and initial state collinear singularities. It also yields a small fraction of the final state collinear singularities.

- Part II a

The transverse momentum vector of the particle 5 is required to have a norm larger than  $p_{Tm}$ , and to belong to a cone  $C_3$  about the direction of particle 3, defined by  $(y_5 - y_3)^2 + (p_{T5} - p_{T3})^2 \leq R_{th}^2$ , with  $R_{th}$  some small arbitrary number.  $C_3$  contains the final state collinear singularities appearing when 5 is collinear to 3.

- Part II b

The transverse momentum vector of the particle 5 is required to have a norm larger than  $p_{Tm}$ , and to belong to a cone  $C_4$  about the direction of particle 4, defined by  $(y_5 - y_4)^2 + (p_{T5} - p_{T4})^2 \leq R_{th}^2$ .  $C_4$  contains the final state collinear singularities appearing when 5 is collinear to 4.

- Part II c

The transverse momentum vector of the particle 5 is required to have a norm larger than  $p_{Tm}$ , and to belong to neither of the two cones  $C_3, C_4$ . This slice yields no divergence, and can thus be treated directly in 4 dimensions.

Collinear and soft singularities appear when integration over the kinematic variables (transverse momentum, rapidity and azimuthal angles) of the particle 5 is performed on parts I, II a and II b. They are first regularized by dimensional continuation from 4 to  $d = 4 - 2\epsilon$ ,  $\epsilon < 0$ . The  $d$ -dimensional integration over the particle 5 on these phase space slices yields these singularities as  $1/\epsilon$  poles together with non singular terms as  $\epsilon \rightarrow 0$ . After combination with the corresponding virtual contributions, the infrared singularities cancel, and the remaining collinear singularities which do not cancel are factorized and absorbed in parton distribution or fragmentation functions. The resulting quantities correspond to pseudo cross sections where the hard partons are unresolved

from the soft or collinear parton 5, which has been "integrated out" inclusively on the parts I, II a, II b. The word "pseudo" means that they are not genuine cross sections, as they are not positive in general. They are split into two kinds. We call pseudo cross section for some  $2 \rightarrow 2$  process the sum of the lowest order term plus the fraction of the corresponding virtual corrections where the infrared and collinear singularities have been subtracted, and which have the kinematics of a genuine  $2 \rightarrow 2$  process. The contributions where the uncanceled collinear singularities are absorbed into parton distribution (on part I) or fragmentation (on parts II a and II b) functions involve an extra convolution over a variable of collinear splitting, as compared to the kinematics of a genuine  $2 \rightarrow 2$  process: we call them pseudo cross sections for quasi  $2 \rightarrow 2$  processes. The detailed content of these terms is given in the Appendix A. For an extended presentation of the details and corresponding explicit formulas, we refer to [15].

As a matter of principle, observables do not depend on the unphysical parameters  $p_{Tm}$  and  $R_{th}$ . Yet, the pseudo cross sections on parts I, II a, II b and II c separately do. Let us briefly discuss the cancellation of the  $p_{Tm}$  and  $R_{th}$  dependences in observables computed according to this method. In the cylindrical part I, the finite terms produced are approximated in order to collect all the terms depending logarithmically on  $p_{Tm}$ , whereas terms proportional to powers of  $p_{Tm}$  are neglected. This differs from the subtraction method implemented in the cylinder in [15], which kept the exact  $p_{Tm}$  dependence. On the other hand, in the conical parts II a and II b, the same subtraction method as in [15] is used, so that the exact  $R_{th}$  dependence is kept. This ensures the exact cancellation of the dependence on the unphysical parameter  $R_{th}$  between part II c and parts II a, II b whereas only an approximated cancellation of the unphysical parameter  $p_{Tm}$  dependence between parts II c, II a and II b and part I occurs. The parameter  $p_{Tm}$  must be chosen small enough with respect to  $p_{T3}$  and  $p_{T4}$  in order that the neglected terms can be safely dropped out. In practice, it has been verified that  $p_{Tm}$  values of the order of half a percent of the minimum of  $p_{T3}$  and  $p_{T4}$  fulfill these requirements. A more detailed discussion on this issue is provided in Appendix B.

The pseudo cross sections on parts I, II a, II b, as well as the transition matrix elements on the part II c, are then used to sample unweighted kinematic configurations, in the framework of a partonic event generator, described in 2.2.2 below.

## 2.2.2 Partonic event generator

For practical purposes, a partonic event generator has been built for diphoton production including all the mechanisms: the "direct", "one-" and "two fragmentation". Each mechanism is treated separately. Firstly, the contribution of a given mechanism to the integrated cross section is calculated with the integration package BASES [18]. At this stage, some kinematic cuts (e.g. on the rapidity of the two photons, on their transverse momenta, etc.) may be already taken into account. Then, for the  $2 \rightarrow 2$  contributions and the quasi  $2 \rightarrow 2$  contributions on the parts I, II a and II b, and the inelastic contributions on the part II c of the phase space, partonic events are generated with SPRING [18] with a weight  $\pm 1$  depending on the sign of the integrand at this point of the phase space<sup>4</sup>. All the events are subsequently stored into a NTUPLE [19]. Finally these NTUPLES can be histogrammed at will, incorporating any further cuts, such as those imposed by some isolation

---

<sup>4</sup>This trick circumvents the fact that SPRING works only with positive integrands, while the pseudo cross sections are not positive. The generated events are thus unweighted up to a sign.

criterion as discussed in the next subsection. It is suitable to use values for  $R_{th}$  and  $p_{Tm}$  which are fairly small and disconnected from any physical parameter. The phase space generation is then as exclusive as possible. Moreover it allows to investigate the dependence of various observables with respect to the physical isolation parameters, as well as to investigate different types of isolation criteria, using an event sample conveniently generated once for all. In practice however one cannot use too small values in order to keep statistical fluctuations under control, unless the computer time and the sizes of the NTUPLES become intractably large.

Let us state more clearly what we mean by partonic event generator. Since the events associated to the  $2 \rightarrow 2$  and quasi- $2 \rightarrow 2$  contributions have a negative weight, this code, properly speaking, is not a genuine event generator on an event-by-event basis. By events, we mean final state partonic configurations. For a given event, the informations stored into the NTUPLE are the 4-momenta of the outgoing particles; their flavors: parton (i.e. quark or gluon) or photon; in the fragmentation cases, the longitudinal fragmentation variable(s) associated with the photon(s) from fragmentation; and, for practical purpose, a label which identifies the type of pseudo cross section ( $2 \rightarrow 2$ , quasi- $2 \rightarrow 2$ , inelastic) which produced the event stored. Notice also that in the fragmentation cases, all but the longitudinal information on the kinematics of the residue of the collinear fragmentation is lost. Hence this type of program does not provide a realistic, exclusive portrait of final states as given by genuine, full event generators like PYTHIA [20] or HERWIG [21]. On the other hand, the latter are only of some improved leading logarithmic accuracy. Thus, our code is more precisely a general purpose computer program of Monte-Carlo type, whose virtue is the computation of various inclusive enough observables within the same calculation, at NLO accuracy.

### 2.3 The implementation of isolation cuts

Collider experiments at SpS, the Tevatron, and the forthcoming LHC do not measure inclusive photons. Indeed, the inclusive production rates of high  $p_T$   $\gamma$ ,  $Z$ ,  $W$ , or of pairs  $\gamma\gamma$  or  $ZZ$ , etc, with large invariant mass, are orders of magnitudes larger than for direct photons. In order to reject the huge background of secondary photons produced in the decays of these mesons, the experimental event selection of direct photons (single photons, as well as diphotons) requires the use of isolation cuts. Such a requirement will be absolutely crucial at LHC for the search of Higgs bosons in the two photon channel and the mass range 90-140 GeV, since the expected background from  $\gamma\gamma$ , etc. is about eight orders of magnitudes larger than the signal before any isolation cut is applied.

A widely used criterion to isolate photons is schematically the following<sup>5</sup>. A photon is said to be isolated if, inside a cone centered around the photon direction in the rapidity and azimuthal angle plane, the amount of hadronic transverse energy  $E_T^{had}$  deposited is smaller than some value  $E_{Tmax}$  fixed by the experiment:

$$(\Delta\eta)^2 + (\Delta\phi)^2 \leq R^2 \quad \text{and} \quad E_T^{had} \leq E_{Tmax} \quad (1)$$

The topic of the isolation of photons based on the above cone criterion (1) has been rather extensively discussed in the theoretical literature, especially in the case of production of single

<sup>5</sup>An alternative to the criterion (1) has been recently proposed in [22], in which the veto on accompanying hadronic transverse energy is the more severe, the closer the corresponding hadron to the photon direction. It has been designed to make the "fragmentation" contribution vanish in an infrared safe way.

isolated photons in hadronic<sup>6</sup> collisions [23, 24, 25, 26, 27]. Beside the rejection of the background of secondary photons, the isolation requirement also reduces the photons from fragmentation. The account of isolation effects on the "fragmentation" contribution was accurate to LO accuracy in [23, 24]. A treatment to NLO accuracy has been subsequently given in [26], following the subtraction framework presented in [25]. Isolation implies however that one is not dealing with inclusive quantities anymore. This raised questions concerning the validity of the factorization property in this case, and whether the fragmentation functions may depend on the isolation parameters, as assumed in [25]. This raised also issues regarding soft gluon divergences in isolated photons cross sections, as in [29]. These questions have been clarified in [27, 30]. The factorization property of collinear singularities still holds for cross sections based on the criterion<sup>7</sup>, and the fragmentation functions involved there are the same as in the inclusive case, whereas the effects of isolation are consistently taken into account in the short distance part. Yet cross sections defined with this criterion may have infrared divergences – or, at least, instabilities, depending on the inclusiveness of the observable considered – located at some isolated critical points inside the physical spectrum of some observables calculated at fixed order, namely NLO, accuracy. This means that the vicinities of these critical points are sensitive to multiple soft gluon effects, which have to be properly taken into account in order to provide correct predictions.

In the present calculation, as in [26, 27] for the case of single photon production, the transverse energy deposited in the cone may come from the residue of the fragmentation, from the parton 5 (which never fragments into photons) or from both. During the projection of the NTUPLES onto any desired observable, the isolation criterion (1) about the two photons is applied to each stored partonic configuration. The effects of isolation are commented in 3.2.2. In addition, at the NLO accuracy at which our calculation is performed, potentially large logarithmic contributions of infrared origin may be induced by the extra isolation constraint on the phase space. The issue of infrared sensitivity induced by isolation will be discussed further in 4.2. Let us mention that no summation of such logarithms is performed in our treatment.

### 3 Phenomenology

In this section, we adopt a LHC oriented presentation. We start with a brief comparison of our NLO calculations with WA70 and D0 data for illustrative purposes. We then show some predictions for LHC in the invariant mass range  $80 \text{ GeV} < m < 140 \text{ GeV}$  corresponding to the Higgs boson search through  $h \rightarrow \gamma\gamma$ . We discuss the ambiguities plaguing these predictions due to the arbitrariness in the choices of the renormalization scale  $\mu$ , of the initial state factorization scale  $M$  (which enters in the parton distribution functions), and of the fragmentation scale  $M_f$ .

#### 3.1 Comparison with experimental data

---

<sup>6</sup>The related topic of isolated prompt photons produced in  $e^+e^-$  annihilation into hadrons has also been abundantly discussed. A variant of the definition (1) suitable for  $e^+e^-$  has been studied in [28], and recently revisited in [29, 30]. An alternative criterion has been proposed in [31], and applied to the measurement of isolated photons in LEP experiments.

<sup>7</sup>The fact that transverse energies are involved in (1) in hadronic collisions is crucial in this respect. Factorization would be broken if energies were used instead.

### 3.1.1 Fixed target data

A comparison between the diphoton differential cross section versus each photon's transverse momentum measured by the WA70 collaboration [1] and our NLO prediction is shown on Fig. 1, together with the respective magnitude of the various contributions. The NLO calculation has been made with the ABFW parton distribution functions [32] for the proton and the corresponding ones for the pion [33]<sup>8</sup>, for the scale choice<sup>9</sup>  $M = M_f = \sqrt{s} = (p_T(1) + p_T(2))$ , with  $\alpha_s = 0.275$ . The "one fragmentation" contribution is one order of magnitude below the "two direct" contribution. The "two fragmentation" contribution is even smaller and negligible here. The smallness of these contributions is the reason why previous works [7, 8] described this observable reasonably well too, despite the absence of higher order corrections to the fragmentation contributions there.

Various correlations between the two photons: the distribution of the  $p_T$  imbalance variable  $z = p_T(1)p_T(2)/p_T^2(1)$ , the distribution of the azimuthal angle between the two photons ( $\phi$ ), the distribution of  $p_{out}$ <sup>10</sup>, and the distribution of transverse momentum of diphotons ( $q_T$ ), have been measured also by the WA70 collaboration [2]. These distributions are infrared sensitive near the elastic boundary of the spectrum (e.g.  $q_T \rightarrow 0$  or  $\phi \rightarrow 0$ ) or near a critical point (e.g.  $z = 1$ ) and, moreover, are quite sensitive to non perturbative effects appearing in the resummed part of calculations summing soft gluon effects. This sensitivity extends over a wide part of the spectrum covered by the measurements. Consequently we do not present any comparison of these data points with the approximation of fixed order accuracy of this work; nor will we discuss the scale ambiguities at fixed target energies.

### 3.1.2 Tevatron collider data

A preliminary study of diphotons events in the central region ( $|\eta(1,2)| < 1.0$ ) has been recently performed by the D0 collaboration [6].

The experimental cuts in the D0 data used for the comparisons are not corrected for electromagnetic calorimeter absolute energy scale. The electromagnetic energy scale correction is given by [6]:

$$E(\text{measured}) = E(\text{true}) +$$

<sup>8</sup>The choice of the parton distributions is mandated by the fact that the initial state of the reaction is a proton. Therefore a consistent set of parton densities inside the proton and the pion must be taken. Indeed, to extract the parton distribution functions in the pion, reactions such as  $p \rightarrow X$  (Drell-Yan) and  $p \rightarrow X$  (direct photon) are used. Consequently some correlations between the proton and the pion partonic densities exist, and it is preferable to use consistent sets in the calculations. Only three groups provided such a work: ABFW [33], MRS [34] and GRV [35]. All these works are rather old and the partonic densities are rather similar in the WA70 x range.

<sup>9</sup>One shall not attach importance to the somewhat unusual value  $\alpha_s = 0.275$  of the scale choice. Relatively low scales such as this one, or  $\alpha_s = 0.25$  equally well, turn out to match the data better than higher scale choices. Yet this particular value was not chosen as the one which matches the data the best, but for a minor though cumbersome computational reason. The WA70 collaboration requires the transverse momenta of the photons to be larger than 3 GeV and 2.75 GeV respectively. However for computational convenience we first implemented a symmetric cut on the  $p_T$  of each photon:  $p_T > 2.75$  GeV at the level of the Monte Carlo generation of photon pairs. In the ABFW parametrizations, the factorization scale  $M^2$  has to be larger than  $2 \text{ GeV}^2$ . Given the above symmetric cut on both photons in the Monte Carlo generation, taking  $\alpha_s = 1/4$  does not ensure that  $M^2$  is always above  $2 \text{ GeV}^2$ , while the choice  $\alpha_s = 0.275$  does.

<sup>10</sup>The beam axis together with the direction of one of the two photons define a plane. The component of the transverse momentum of the other photon along the direction perpendicular to this plane is the  $p_{out}$  of this photon.

where

$$\begin{aligned}
 &= 0.9514 \pm 0.0018^{+0.0061}_{-0.0017} \\
 &= 0.158 \pm 0.015^{+0.003}_{-0.021} \text{ GeV}
 \end{aligned}$$

Thus, the experimental cuts at measured values of 14 (respectively 13) GeV correspond to cuts at roughly 14.90 (resp. 13.85) GeV in the theoretical calculation. Smearing effects accounting for electromagnetic calorimeter resolution have not been implemented, but given the experimental fractional energy resolution of the electromagnetic calorimeter [36], they are expected to be of the level of a few percent only.

The actual isolation cuts used experimentally (such as vetoes on charged tracks in some conical vicinity about each photon, etc.) are quite more complicated than the schematic criterion (1), and cannot be faithfully implemented at the partonic level. We instead simulated them in our NLO calculation by requiring that the accompanying transverse partonic energy be less than  $E_{T \text{ max}} = 2$  GeV in a cone  $R = 0.4$  about each photon. Varying  $E_{T \text{ max}}$  from 1 to 3 GeV in the calculated cross-section, as a rough estimate of the effects of smearing due to hadronic calorimeter resolution and unfolding of underlying events contribution turns out to have a less than 4% effect.

The MRST2 set of parton distributions functions<sup>11</sup> [37] is used<sup>12</sup>, with the scales arbitrarily chosen to be  $M = M_f = m = 2$ . The prediction for the above scale choice is shown for the diphoton differential cross sections vs. the transverse momentum of each photon (Fig. 2), the diphoton mass (Fig. 3), and for the transverse momentum of photon pairs (Fig. 4) and the azimuthal angle between the photons (Fig. 5). With the scale choice used, the "one fragmentation" contribution is roughly one tenth of the "direct" one whereas the "two fragmentation" yields a tiny contribution. To illustrate this, the different contributions: "direct", "one-" and "two fragmentation" are shown separately on Fig. 5. The distributions of the transverse momentum of photon pairs and of the azimuthal angle between the photons are well known to be controlled by multiple soft gluon emission near the elastic boundary of the spectrum,  $q_T \neq 0$  and  $\phi \neq 0$  respectively. Consequently, the accuracy of any fixed-order calculation, including the present one, is not suited to study such observables in these respective ranges. More on this issue will be commented in the next section. On the other hand a NLO calculation is expected to be predictive for the tails of these distributions away from the infrared sensitive region.

The data are reasonably described, taking into account a correlated systematic error for events in which the  $p_T$  of both photons is above 20 GeV. This correlated systematic error due to the background evaluation affects obviously the three highest  $p_T$  points of the transverse energy spectrum, as well as the three highest points of the diphoton mass spectrum.

---

<sup>11</sup>The MRST sets 1,2,3 are associated with the value  $\frac{1}{M_S} = 300$  MeV for  $n_f = 4$  flavors. This corresponds to  $s(m_Z) = 0.1175$  in the  $\overline{MS}$  scheme. For more details, see [37]

<sup>12</sup>The MRST1 set is presented by the authors of [37] as the default set. However, in order to take into account mutually inconsistent data sets on single direct photon production at fixed targets, a  $k_T$  smearing procedure is involved in the determination of this set. This procedure is strongly model dependent and questionable as long as no unambiguous way is found to lodge it in the QCD improved parton model. The set MRST2 does not involve this procedure, so we prefer to base any prediction and comparison on this set.

We do not present any analysis of the various scale dependences for Tevatron. Such a discussion is proposed for LHC in the next section. Yet let us mention that, at Tevatron, the energy scale is lower and the relevant values of  $x$  are somewhat higher than at LHC. Consequently, the renormalization scale dependence is slightly sharper, on the other hand the factorization scale dependence is somewhat flatter than at LHC. Nevertheless the situation at Tevatron is expected to be qualitatively similar to the one at LHC.

## 3.2 Predictions for LHC

We now discuss some results computed with the kinematic cuts from the CMS and ATLAS proposals [40], namely  $p_T(\gamma_1) > 40 \text{ GeV}$ ,  $p_T(\gamma_2) > 25 \text{ GeV}$ ,  $|\eta(\gamma_{1,2})| < 2.5$ , with  $80 \text{ GeV} < m < 140 \text{ GeV}$ , and using the MRST2 set of parton distribution functions [37] and the fragmentation functions of [10].

### 3.2.1 Scale ambiguities

We first consider the invariant mass distribution of diphotons, in absence of isolation cuts, cf. Fig. 6 in order to illustrate the strong dependence of the splitting into the three contributions, "direct", "one-fragmentation" and "two-fragmentation", on the scale chosen, as we warned in 2.1. In both choices of scales displayed the "one-fragmentation" contribution dominates, but the hierarchy between "direct" and "two-fragmentation" contributions is reversed from one choice to the other. With the choice of scales  $M = M_f = m = 2$ , the "one-fragmentation" is more than twice larger than the "direct" one, and the "two-fragmentation" is the smallest. On the other hand, with the other choice  $M = M_f = 2m$ , the "one-fragmentation" contribution is three to five times larger than the "two-fragmentation" component, and more than one order of magnitude above the "direct" one. On the other hand the total contribution seems rather stable.

Yet the arbitrariness in the choices of the various scales still induces theoretical uncertainties in NLO calculations. In the following we actually do not perform a complete investigation of all three scale ambiguities independently with search for an optimal region of minimal sensitivity. At the present stage, we limit the study to an estimation of the pattern and magnitude of their effect on our results. We show how the scale ambiguities affect our prediction for the invariant mass distribution. We consider both the case without isolation (Fig. 7) and the isolated case with  $E_{T \text{ max}} = 5 \text{ GeV}$  inside  $R = 0.4$  (Fig. 8). For the present purpose, the virtue of the actual values of the isolation parameters used here is to strongly suppress the fragmentation contributions hence the associated  $M_f$  dependence. We compare four different choices of scales: two choices along the first diagonal  $= M = M_f = m = 2$  and  $= M = M_f = 2m$ ; and two anti-diagonal choices,  $= m = 2; M = M_f = 2m$  and  $= 2m; M = M_f = m = 2$ . We do not perform a separate study of fragmentation scale dependence. Yet the latter can be indirectly estimated by comparing the results of the isolated case, where the fragmentation components, thereby the corresponding fragmentation scale dependence, are strongly suppressed, with the situation in the non isolated case, where especially the "one-fragmentation" contribution is quite large, and the "two-fragmentation" not negligible, so that the issue of fragmentation scale dependence matters.

When scales are varied between  $m = 2$  and  $2m$  along the first diagonal  $= M = M_f$ , the NLO results for the invariant mass distribution appear surprisingly stable, since they change by

about 5% only. Alternatively, anti-diagonal variations of  $\mu$  and  $M = M_f$  in the same interval about the central value  $\mu$  lead to a variation still rather large (up to 20% cf. Fig. 7 and Fig. 8). This is because variations with respect to  $\mu$  and  $M$  are separately monotonous but act in opposite ways. When  $\mu$  is increased,  $\sigma_s(\mu^2)$  hence the NLO corrections decrease<sup>13</sup>. On the other hand the relevant values of momentum fraction of incoming partons are small,  $x \ll 1$  ( $10^{-3}$  to  $10^{-2}$ ) so that the gluon and sea quark distribution functions increase when  $M$  is increased. In the isolated case, this leads to a monotonous increase of the "direct" component, over a large band of the invariant mass range considered, as  $M$  is increased, cf. Fig. 9, which is induced in particular by the monotonous increase of the box contribution. Scale changes with respect to  $\mu$  and  $M$  turn out to nearly cancel against each other along the first diagonal but add up in the other case. Actually, the stability along the first diagonal is accidental.

In conclusion, the  $\mu, M$  dependences are thus not completely under control yet at NLO in the kinematic range considered. On the opposite, the account for the NLO corrections to the fragmentation components provides some stability with respect to  $M_f$  variations about orthodox choices of the fragmentation scale.

The issue of  $\mu$  dependence of less inclusive observables, such as the tails of the  $q_T$  or distributions are the same for the invariant mass distribution. This is because the tails of these distributions is purely given by the NLO corrections and dominated by the  $O(\mu^2)$  corrections of the "two direct" component. On the other hand, the  $M$  dependence is a bit larger, so is the combined uncertainty on the theoretical results for these distributions, cf. Fig. 10 and Fig. 11.

### 3.2.2 Effect of isolation

We now consider the effect of isolation on the various contributions. As expected, isolation reduces the diphoton production rate, with respect to the inclusive case, cf. Fig. 12. More precisely, severe isolation requirements like  $E_{T, \max} = 5 \text{ GeV}$  inside a cone  $R = 0.4$  suppress the "one fragmentation" component, which dominates the inclusive rate, by a factor 20 to 50, and kill the "two fragmentation" contribution completely.

However this net result hides a rather intricate mechanism, cf. Fig. 13 vs. Fig. 6, by which the "two direct" contribution turns out to be increased! Surprising as it may seem at first sight, this effect has the following origin. Higher order corrections to the "two direct" component involve in particular the two subprocesses  $q\bar{q} \rightarrow g$  and  $gq \rightarrow q$  (where  $q$  is a quark or an antiquark). The first one yields a positive contribution. On the other hand, the collinear safe part of the second one yields a contribution which is negative, and larger in absolute value than the previous one in the inclusive case, as was already seen in [7]. Isolation turns out to suppress more the higher

<sup>13</sup> In processes for which the lowest order is proportional to some power  $\mu^n; n \geq 1$ , an explicit  $\mu$  dependence appears in the next-to-leading order coefficient function, which partially compensates the (large)  $\mu$  dependence in  $\sigma_s(\mu^2)$  weighting the lowest order. Unlike this, in the "two direct" component which dominates the cross section when a drastic isolation is required, the lowest order involves no  $\mu$ . This leads to a rather small  $\mu$  dependence, since the latter starts only at NLO. On the other hand, the  $\mu$  dependence occurs only through the monotonous decrease of the  $\sigma_s(\mu^2)$  weighting the first higher order correction: there is no partial cancellation of  $\mu$  dependence. Such cancellation would start only at  $O(\mu^2)$ , i.e. at NNLO. The mechanism is more complicated in presence of fragmentation components, and the situation becomes mixed up between all components when the severity of isolation is reduced.

order corrections from the second mechanism than from the first one, so that the NLO isolated "two direct" contribution is larger than the inclusive one. Yet, the "fragmentation" contributions are suppressed more than the "two direct" one is increased, so that the sum of all contributions is indeed decreased, with respect to the inclusive case. Once again, one has to remember that the splitting into the three mechanisms depend, not only on the factorization scale, but more generally on the factorization scheme. This arbitrariness generates such counterintuitive oscillations; in a final state factorization scheme different than the  $\overline{MS}$  scheme, the various components, especially the "two direct" one, may be separately affected by isolation cuts in a different way. This once more illustrates the danger of playing with these unphysical quantities separately.

A more detailed analysis of the dependence of NLO estimations of various observables on the isolation cut parameters, especially on  $E_{Tmax}$  will be given in a forthcoming publication. We will also come back to this issue, regarding infrared sensitivity, in 4.3.

## 4 Infrared sensitive observables of photon pairs and soft gluon divergences.

Being based on a fixed, finite order calculation, our computer code is not suited for the study of observables controlled by multiple soft gluon emission, and has to be improved in this direction. Among these infrared sensitive observables, one may distinguish the following examples, most of which would require an improved account of soft gluon effects.

### 4.1 Infrared sensitivity near the elastic boundary

#### 4.1.1 The transverse momentum distribution $d = d_{q_T}$ of photon pairs near $q_T = 0$

Both in the inclusive and isolated cases, this distribution is an infrared sensitive observable, controlled by the multiple emission of soft and collinear gluons. This well known phenomenon has been extensively studied for the corresponding observable in the Drell-Yan process [41]. A loss of balance between the contribution of real emission, strongly suppressed near this exclusive phase space boundary, and the corresponding virtual contribution, results in large Sudakov-type logarithms of  $m^2 = q_T^2$  ( $m$  being the invariant mass and  $q_T$  the transverse momentum of the photon pair – the heavy vector boson in the Drell-Yan case) at every order in perturbation. In order to make sensible predictions in this regime, these Sudakov-type logarithms have to be resummed to all orders.

The treatment of the "two direct" and box contributions is similar to the well known Drell-Yan process, and has been carried out recently by [42] at next-to-leading logarithmic accuracy in the framework tailored by Collins, Soper and Sterman [43]. On the other hand, the fragmentation contributions do not diverge order by order when  $q_T \rightarrow 0$ . Indeed, in the "one fragmentation" case,

$$\text{parton}_1 + \text{parton}_2 \rightarrow \text{parton}_1 + \text{parton}_3 \quad (2)$$

$$\text{parton}_3 \rightarrow \text{parton}_2 + X \quad (3)$$

the NLO contribution to the hard subprocess (2) yields a double logarithm of the form

$$s \ln^2 k p_T (\text{parton}_1) + p_T (\text{parton}_3) k \quad (4)$$

when  $k_{p_T(1)} + p_T(\text{parton}_3) \neq 0$ . However the extra convolution associated with the fragmentation (3) involves an integration over the fragmentation variable  $p_T(2) = p_T(\text{parton}_3)$  which smears out this integrable singularity. The "two fragmentation" contribution involves two such convolutions, hence one more smearing.

#### 4.1.2 The distribution of photon-photon azimuthal angle $d = d_{\text{near}} =$

This distribution is another interesting infrared sensitive observable, measured by several experiments both at fixed target and collider energies [2, 5, 6], though less discussed in the literature from the theoretical side. The regime  $\theta \rightarrow 0$  includes back-to-back photons, a set of configurations which lie at the elastic boundary of the phase space. This case differs from the previous one for two reasons. Firstly, not only the "two direct" contribution diverges order by order when  $\theta \rightarrow 0$ , but also both "one-" and "two fragmentation" contributions diverge as well, as can be inferred from Fig. 5. Indeed, consider the example of the "one fragmentation case", cf. equations 2 and 3. Selecting  $\theta \rightarrow 0$  emphasizes the configurations with  $p_T(\text{parton}_3) \rightarrow p_T(1) \neq 0$ , so that all the emitted partons besides parton 3 have to be collinear to either of the incoming or outgoing particles, and/or soft, which yields double logarithms

$$s \ln^2 [ (p_{T(3)} - p_{T(1)}) ] \quad (5)$$

associated with each of the hard partons 1;2;3 - plus single logarithms as well. For the observable  $d = d_{\text{near}} =$ , the integral involved in the convolution of the hard subprocess with the fragmentation functions does not smear these logarithmic divergences, since the fragmentation variable  $p_T(2) = p_T(\text{parton}_3)$  is decoupled from the azimuthal variable  $p_T(\text{parton}_3)$  which is equal to  $p_T(2)$ , 2 and parton 3 being collinear. A similar observation holds for the "two fragmentation" component. Moreover, in both fragmentation cases, soft gluons may couple to both initial and final state hard emitters. The resulting color structure of the emitters is more involved than in the "two direct" case, and especially more complicated in the "two fragmentation" case as shown in some recent works [44]. This would make any resummation quite intricate beyond leading logarithms.

Let us notice that both fragmentation components make  $d = d_{\text{near}} =$  diverge also when  $\theta \rightarrow 0$ . The increase of the fragmentation contributions in the lower  $\theta$  range is the trace of this divergence, cf. Fig. 5.

#### 4.2 An infrared divergence inside the physical region.

In the case of photons isolated with the standard fixed cone size criterion of eqn. (1), a new problem appears in the  $q_T$  distribution. This problem does not concern the region  $q_T \neq 0$ ; still it has to do with infrared and collinear divergences. This can be seen on Fig. 14, which shows the observable  $d = d_{q_T}$  vs.  $q_T$  for isolated photon pairs, computed at NLO accuracy. The computed  $q_T$  distribution turns out to diverge when  $q_T \rightarrow E_{T \text{ max}}$  from below. Notice that the critical point  $E_{T \text{ max}}$  is located inside the physical region. The phenomenon is similar to the one discovered in [25] in the production of isolated photons in  $e^+e^-$  annihilation, and whose physical explanation has been given in [30] following the general framework of [45]. It is a straightforward exercise to see that the lowest order "one fragmentation" contribution has a stepwise behaviour, as noticed in [9]. Indeed, at this order, the two photons are back-to-back.  $E_{T \text{ had}}$  being the transverse hadronic energy deposited in the

cone about the photon from fragmentation, the conservation of transverse momentum implies at this order that  $E_{T \text{ had}} = q_T$ . The corresponding contribution to the differential cross section  $d = dq_T$  thus takes the schematic form :

$$\frac{d}{dq_T} \text{ (1 fragm ; LO)} = f(q_T) (E_{T \text{ max}} - q_T) \quad (6)$$

According to the general analysis of [45], the NLO correction to  $d = dq_T$  has a double logarithmic divergence at the critical point  $q_T = E_{T \text{ max}}$ <sup>14</sup>. The details of this infrared structure are very sensitive to the kinematic constraints and the observable considered. In the case at hand, at NLO,  $d = dq_T$  gets a double logarithm below the critical point, which is produced by the convolution of the lowest order stepwise term above, with the probability distribution for emitting a soft and collinear gluon:

$$\frac{d}{dq_T} \text{ (1 fragm ; HO)} = f(q_T) (E_{T \text{ max}} - q_T) \left[ \frac{s}{2} C \ln^2 \left( 1 - \frac{q_T^2}{E_{T \text{ max}}^2} \right) + \right] \quad (7)$$

where  $C$  is a color factor,  $C_F$  or  $N_c$  according to whether the soft collinear gluon emitter is a quark (antiquark) or a gluon. More generally, at each order in  $s$ , up to two powers of such logarithms will appear, making any fixed order calculation diverge at  $q_T = E_{T \text{ max}}$ , so that the spectrum computed by any fixed order calculation is unreliable in the vicinity of this critical value. An all order resummation has to be carried out if possible in order to restore any predictability. A correlated step appears also in the "two direct" contribution at NLO, in the bin about  $q_T = E_{T \text{ max}}$ . A detailed study of these infrared divergences will be presented in a future article.

No such divergence appears in the  $q_T$  distribution of photon pairs presented in [9]. The non appearance of the double logarithmic divergence there comes from the fact that the latter pops out only at NLO, while the authors of [9] compute the "one fragmentation" component at lowest order. Furthermore, the stepwise lowest order "one fragmentation" contribution to the  $q_T$  distribution is replaced in [9] by the result of the Monte Carlo simulation of this component using PYTHIA [20]. A quantitative comparison is thus difficult to perform<sup>15</sup>.

<sup>14</sup>In practice, the  $q_T$  spectrum is sampled into bins of finite size, and the distribution represented on Fig. 14 is averaged on each bin. Since the logarithmic singularity is integrable, no divergence is actually produced. However when the bin size is shrunk, the double logarithmic branch appears again.

<sup>15</sup>Such a comparison involves two issues.

The first aspect concerns the infrared sensitivity below the critical point. When the scale of  $s$  in the Sudakov factor of the fragmenting quark is chosen to be the transverse momentum of the emitted gluon with respect to the emitter, the parton shower not only reproduces the fragmentation function of a parton into a photon to the collinear leading logarithmic approximation, but it also provides an effective resummation of soft gluons effects to infrared and collinear leading logarithmic accuracy. (This would not be true if, instead, the scale of  $s$  in the Sudakov factor were the virtuality of the emitter). This ensures that the distribution does not diverge from below at the critical point, but rather tends to a finite limit.

The second issue concerns the shape of the tail of this contribution above the critical point. Indeed, energy-momentum conservation at each branching makes the parton shower generate also contributions in the region  $q_T > E_{T \text{ max}}$ , which is forbidden at lowest order. These contributions would be classified in a beyond leading order calculation as higher order corrections. Unlike in a fixed order calculation however, they provide only a partial account of such corrections, but to arbitrary high order. The accuracy of these terms is thus uneasy to characterize, and a quantitative comparison between PYTHIA and any fixed order calculation is difficult to perform.

It can be noticed that the divergence at  $q_T = E_{T \text{ max}}$  is not visible on Fig. 4. This is because in this case, the critical point  $E_{T \text{ max}}$  in the  $q_T$  spectrum where the theoretical calculation diverges is too close to the other singular point  $q_T = 0$ , given the binning used. The two singularities contribute with opposite signs in these bins and a numerical compensation occurs, resulting in no sizeable effect. Yet the problem is only camouflaged. A similar smearing appears also at LHC energies for a stringent isolation cut, cf. Fig. 10.

### 4.3 Reliability of NLO calculations with stringent isolation cuts

Let us add one more comment concerning NLO partonic predictions with very stringent isolation cuts. In such calculations, the isolation cuts act on the products of the hard subprocess only. On the other hand, in an actual LHC event, a cut as severe as  $E_{T \text{ max}} = 2.5 \text{ GeV}$  inside a cone  $R = 0.3$  or  $0.4$  will be nearly saturated by underlying events and pile up.

This means that such an isolation cut actually allows almost no transverse energy deposition from the actual hadronic products of the hard process itself. This may be most suitable experimentally, and one may think about simulating such an effect safely in an NLO partonic calculation by using an effective transverse energy cut much more severe than the one experimentally used. However, requiring that no transverse energy be deposited in a cone of fixed size about a photon is not infrared safe, i.e. it would yield a divergent result order by order in perturbation theory. This implies that NLO partonic calculations implemented with finite but very stringent isolation cuts in a cone of fixed finite size would lead to unreliable results, plagued by infrared instabilities involving large logarithms of  $E_{T \text{ max}}$ . What is more, these infrared nasties would not be located at some isolated point in the diphoton spectrum (like some elastic boundary or some critical point, as in the previous subsection), but instead they would extend over its totality, even for observables such as the invariant mass distribution. The issue of an all order summation of these logarithms of  $E_{T \text{ max}}$  would have to be investigated in this case.

## 5 Conclusions and perspectives

We presented an analysis of photon pair production with high invariant mass in hadronic collisions, based on a perturbative QCD calculation of full NLO accuracy. The latter is implemented in the form of a Monte Carlo computer programme of partonic event generator type, `DPHOX`. The predictions of this study are in reasonable agreement with both WA70 fixed target, and preliminary D0 collider data, in the kinematical range where the NLO approximation is safe, namely away from the elastic boundary of phase space. Yet more will be learnt from the final analysis of the Tevatron data, and even more so after the Tevatron run II in the perspective of the LHC. It will then be worthwhile to perform a more complete phenomenological study.

This notwithstanding, there remains room for improvements. A first improvement will be to take into account multiple soft gluon effects in order to calculate infrared sensitive observables correctly. Another improvement will concern a more accurate account of contributions beyond NLO, associated namely with the gluon-gluon initiated subprocess. Among those are the NNLO corrections, and even the two loop, so-called double box correction to  $gg \rightarrow \gamma\gamma$ , which may be quantitatively important at LHC for the background to Higgs search.

A better understanding of the effects of isolation, and their interplays with infrared problems is also required. This concerns the  $q_T$  distribution near the critical point  $q_T = E_{T \text{ max}}$  induced by isolation even when  $E_{T \text{ max}}$  is not small; this concerns also the status of partonic predictions when  $E_{T \text{ max}}$  is chosen very small. Alternatively it would be interesting to explore the properties of different isolation criteria, such as, for example, the one invented recently by Frixione [22]. Concerning these last two items, approaches relying on beyond leading order partonic level calculations, and full event generators like PYTHIA or HERWIG will be complementary.

Acknowledgments We acknowledge discussions with J. Womersley and T. O. Montes on the D0 data, J. Owens on theory vs. data comparisons, and C. Balazs about the theoretical ingredients inside the RESBOS code. We thank F. Gianotti, P. Petro, E. Richter-Was and V. Tisserand for discussions concerning the Atlas Proposal. This work was supported in part by the EU Fourth Training Programme "Training and Mobility of Researchers", Network "Quantum Chromodynamics and the Deep Structure of Elementary Particles", contract FMRX-CT 98-0194 (DG 12-M HT).

## A Technical details on the two photon production

In this appendix, we give some details on the method used to deal with infrared and soft divergences. For a complete presentation, we refer to [15]. The most complicated kinematics happens in the two fragmentation mechanism. Only the two fragmentation contribution will be treated in this appendix, the kinematics of the other cases can be simply deduced replacing the fragmentation function by a Dirac distribution:

$$D_{\rightarrow k}(\mathbf{x}; M_f^2) = \delta(1-x)$$

At the hadronic level, the reaction  $H_1(K_1) + H_2(K_2) \rightarrow (K_3) + (K_4) + X$  is considered with:

$$\begin{aligned} K_1 &= \frac{P_S}{p_S^2} (1; 0; 1) \\ K_2 &= \frac{p_S^2}{S} (1; 0; 1) \\ K_3 &= K_{T3} (\cosh y_3; n_3; \sinh y_3) \\ K_4 &= K_{T4} (\cosh y_4; n_4; \sinh y_4) \end{aligned}$$

where

$$n_3^2 = n_4^2 = 1$$

The cross section of the preceding reaction is the sum of the following parts.

- The part I (cf. sect. 2.2.1) contains the infrared, the initial state, and a part of the final state collinear singularities. Once these divergences have been subtracted, i.e. cancelled against virtual divergences or absorbed into the bare parton distribution (for the initial state collinear singularities) or the bare fragmentation functions (for the final state collinear singularities), this part generates three types of finite terms.

- (i) The first type, of infrared origin, has the same kinematics as the lowest order (LO) terms and is given in A.4 Pseudo cross section for the infrared and virtual parts.

- (ii) The second type, of initial state collinear origin, has an extra integration over the center of mass energy of the hard scattering, as compared to LO kinematics. For this reason, it is called quasi  $2!2$ . It is given in A.2 Pseudo cross sections for the initial state collinear parts.
  - (iii) There is also a third type, of final state collinear origin, which involves also an extra integration as compared to LO kinematics.
- The parts II a and II b contain the rest of the final state collinear singularities. Once these divergences have been absorbed into the bare fragmentation functions, the remaining finite terms involve an extra integration over the relative momentum of the collinear partons, as compared to LO kinematics. These terms are combined with those of the so called third type (iii) above, cf. equations (A.10) and (A.11). The resulting contributions are called quasi  $2!2$  as well. They are given in A.3 Pseudo cross sections for the final state collinear parts.
  - The part II c has no divergences. It is given in A.1 Cross section for real emission.

#### A.1 Cross section for real emission

The cross section is parametrized in the following way:

$$\begin{aligned}
 & \int_{x_{3\text{in}}}^Z \int_{x_3}^Z \int_{p_{Tm}}^{p_{T5\text{ax}}} \int_{p_{T5}}^{p_{T4}} d^3K_{T3} d^3K_{T4} \\
 = & C_{ij} \int_{x_{3\text{in}}}^Z \frac{dx_3}{x_3} \int_{p_{Tm}}^{p_{T5\text{ax}}} \frac{dx_4}{x_4} \int_{p_{T5}}^{p_{T4}} \frac{d^3K_{T3}}{p_{T3}} \frac{d^3K_{T4}}{p_{T4}} \int_{x_1}^Z \frac{dx_1}{x_1} \int_{x_2}^Z \frac{dx_2}{x_2} \int_{p_{Tm}}^{p_{T5\text{ax}}} \frac{d^3K_{T5}}{p_{T5}} \int_{p_{T5}}^{p_{T4}} \frac{d^3K_{T4}}{p_{T4}} \int_{p_{T5}}^{p_{T4}} \frac{d^3K_{T5}}{p_{T5}} \int_{p_{T5}}^{p_{T4}} \frac{d^3K_{T4}}{p_{T4}} \\
 & \frac{D_{=1}(x_3; M_f^2)}{p_{T3}} \frac{D_{=1}(x_4; M_f^2)}{p_{T4}} \frac{F_{i=H_1}(x_1; M^2)}{x_1} \frac{F_{j=H_2}(x_2; M^2)}{x_2} \int_{p_{T5}}^{p_{T4}} \frac{d^3K_{T5}}{p_{T5}} \int_{p_{T5}}^{p_{T4}} \frac{d^3K_{T4}}{p_{T4}} \\
 + & \int_{x_{4\text{in}}}^Z \frac{dx_4}{x_4} \int_{p_{Tm}}^{p_{T5\text{ax}}} \frac{dx_3}{x_3} \int_{p_{T5}}^{p_{T4}} \frac{d^3K_{T5}}{p_{T5}} \int_{p_{T5}}^{p_{T4}} \frac{d^3K_{T4}}{p_{T4}} \int_{x_1}^Z \frac{dx_1}{x_1} \int_{x_2}^Z \frac{dx_2}{x_2} \int_{p_{Tm}}^{p_{T5\text{ax}}} \frac{d^3K_{T5}}{p_{T5}} \int_{p_{T5}}^{p_{T4}} \frac{d^3K_{T4}}{p_{T4}} \\
 & \frac{D_{=1}(x_4; M_f^2)}{p_{T4}} \frac{D_{=1}(x_3; M_f^2)}{p_{T3}} \frac{F_{i=H_1}(x_1; M^2)}{x_1} \frac{F_{j=H_2}(x_2; M^2)}{x_2} \int_{p_{T5}}^{p_{T4}} \frac{d^3K_{T5}}{p_{T5}} \int_{p_{T5}}^{p_{T4}} \frac{d^3K_{T4}}{p_{T4}}
 \end{aligned} \tag{A.1}$$

where

$$x_1 = \frac{p_{T3}}{S} e^{y_3} + \frac{p_{T4}}{S} e^{y_4} + \frac{p_{T5}}{S} e^{y_5} \quad (\text{A } 2)$$

$$= x_1 + \frac{p_{T5}}{S} e^{y_5}$$

$$x_2 = \frac{p_{T3}}{S} e^{y_3} + \frac{p_{T4}}{S} e^{y_4} + \frac{p_{T5}}{S} e^{y_5} \quad (\text{A } 3)$$

$$= x_2 + \frac{p_{T5}}{S} e^{y_5}$$

$$x_{3m \text{ in}} = \frac{2K_{T3}}{S} \cosh y_3 \quad (\text{A } 4)$$

$$x_{4m \text{ in}} = \frac{2K_{T4}}{S} \cosh y_4 \quad (\text{A } 5)$$

The transverse momenta  $p_{T3}$  (resp.  $p_{T4}$ ) are the transverse momenta of the fragmenting partons. They are related to the photon variables by  $p_{T3} = K_{T3}=x_3$  (resp.  $p_{T4} = K_{T4}=x_4$ ). The integration range for the pair of variables  $y_3$  (resp.  $y_4$ ),  $y_5$  is the kinematically allowed range minus a cone in rapidity azimuthal angle  $C_3$  (resp.  $C_4$ ) along the  $p_3$  (resp.  $p_4$ ) direction whose size is  $R_{th}$ . The overall factor  $C_{ij}$  reads:

$$C_{ij} = \frac{s^{3/2}(\theta)}{4S^2 C_i C_j}$$

and the  $C_i$  are given by:

$$C_i = \begin{cases} N & \text{for quarks} \\ (N^2 - 1) & \text{for gluons} \end{cases}$$

The matrix element squared<sup>16</sup>, taken from the first reference of [7] and [46], has been split into two parts:

$$\mathcal{M}_{ij}^2 = \mathcal{M}_{ij}^2 + \mathcal{M}_{ij}^2$$

The first part  $\mathcal{M}_{ij}^2$  contains final state collinear singularities arising when  $p_3 \parallel p_5$  and the second part  $\mathcal{M}_{ij}^2$  contains final state collinear singularities arising when  $p_4 \parallel p_5$ . More precisely, the matrix element squared can be written as a weighted sum of eikonal factors  $E_{ab}$  plus a term free of infrared or collinear singularities:

$$\mathcal{M}_{ij}^2|_{\text{kin}} = \sum_{a=1}^4 \sum_{b=a+1}^4 H_{ab}(p_5) E_{ab} + G(p_5) \quad (\text{A } 6)$$

where

$$E_{ab} = \frac{p_a \cdot p_b}{p_a \cdot p_5 p_b \cdot p_5}$$

Using:

$$\frac{1}{p_3 \cdot p_5 p_4 \cdot p_5} = \frac{1}{p_1 \cdot p_5 + p_2 \cdot p_5} \frac{1}{p_3 \cdot p_5} + \frac{1}{p_4 \cdot p_5} \quad (\text{A } 7)$$

we get:

---

<sup>16</sup>An overall factor of the matrix element squared containing the average on spins and colors of the initial state and the coupling constant has been put into the coefficient  $C_{ij}$

$$\mathcal{M}_{\mathbb{B}}^{\mathbb{P}} = \frac{1}{2} H_{12}(\mathbb{P}_5) E_{12} + H_{13}(\mathbb{P}_5) E_{13} + H_{23}(\mathbb{P}_5) E_{23} + H_{34}(\mathbb{P}_5) E_{34}^0 + \frac{1}{2} G(\mathbb{P}_5)$$

$$\mathcal{M}_{\mathbb{A}}^{\mathbb{P}} = \frac{1}{2} H_{12}(\mathbb{P}_5) E_{12} + H_{14}(\mathbb{P}_5) E_{14} + H_{24}(\mathbb{P}_5) E_{24} + H_{34}(\mathbb{P}_5) E_{34}^0 + \frac{1}{2} G(\mathbb{P}_5)$$

with

$$E_{34}^0 = \frac{\mathbb{P}_3 \mathbb{P}_4}{\mathbb{P}_1 \mathbb{P}_5 + \mathbb{P}_2 \mathbb{P}_5} \frac{1}{\mathbb{P}_3 \mathbb{P}_5}$$

$$E_{34}^0 = \frac{\mathbb{P}_3 \mathbb{P}_4}{\mathbb{P}_1 \mathbb{P}_5 + \mathbb{P}_2 \mathbb{P}_5} \frac{1}{\mathbb{P}_4 \mathbb{P}_5}$$

In order that the infrared divergences cancel, and the collinear singularities factorize out, the coefficients  $H_{ab}$  have to fulfill:

$$\frac{C_i}{C_{i^0}} a_{i^0 i}^{(d)}(z_1) \mathcal{M}_{\mathbb{A}^0 j^0 k^1}^{\mathbb{P}B} =$$

$$z_1 H_{12}(1-z_1) p_1 + H_{13}(1-z_1) p_1 + H_{14}(1-z_1) p_1$$

$$\frac{C_j}{C_{j^0}} a_{j^0 j}^{(d)}(z_2) \mathcal{M}_{\mathbb{A}^0 j^0 k^1}^{\mathbb{P}B} =$$

$$z_2 H_{12}(1-z_2) p_2 + H_{23}(1-z_2) p_2 + H_{24}(1-z_2) p_2$$

$$a_{kk^0}^{(d)}(z_3) \mathcal{M}_{\mathbb{A}^0 j^0 k^1}^{\mathbb{P}B} = \quad \#$$

$$z_3 H_{13} \frac{1-z_3}{z_3} p_3 + H_{23} \frac{1-z_3}{z_3} p_3 + H_{34} \frac{1-z_3}{z_3} p_3$$

$$a_{ll^0}^{(d)}(z_4) \mathcal{M}_{\mathbb{A}^0 j^0 k^1}^{\mathbb{P}B} = \quad \#$$

$$z_4 H_{14} \frac{1-z_4}{z_4} p_4 + H_{24} \frac{1-z_4}{z_4} p_4 + H_{34} \frac{1-z_4}{z_4} p_4$$

In particular, the cancellation of infrared divergences is insured by:

$$H_{12}(0) + H_{13}(0) + H_{14}(0) = a_{ii}^{(d)}(1) \mathcal{M}_{\mathbb{A}^0 j^0 k^1}^{\mathbb{P}B}$$

$$H_{12}(0) + H_{23}(0) + H_{24}(0) = a_{jj}^{(d)}(1) \mathcal{M}_{\mathbb{A}^0 j^0 k^1}^{\mathbb{P}B}$$

$$H_{13}(0) + H_{23}(0) + H_{34}(0) = a_{kk}^{(d)}(1) \mathcal{M}_{\mathbb{A}^0 j^0 k^1}^{\mathbb{P}B}$$

$$H_{14}(0) + H_{24}(0) + H_{34}(0) = a_{ll}^{(d)}(1) \mathcal{M}_{\mathbb{A}^0 j^0 k^1}^{\mathbb{P}B}$$

The functions  $a_{ij}^{(d)}(z)$  will be given in equation (A.13).

In equation (A.1), the integration domain for the rapidities and the transverse momenta of the two photons is in general limited by experiments. The integration over  $p_{T5}$  is constrained by:

$$p_{T5}^2 < S(1-x_1)(1-x_2):$$

## A.2 Pseudo cross sections for the initial state collinear parts

The finite part associated to the collinear divergence  $p_1 // p_5$  is given by:

$$\begin{aligned}
 \Gamma_{5=1} &= \int_{x_{3m}^0}^z \int_{x_{4m}^0}^z \int_{x_3^0}^z \int_{x_4^0}^z \frac{dx_3}{x_3} \frac{dx_4}{x_4} \\
 &\frac{s^{(2)}}{2} C_{ij}^B P_T (p_{T3} p_{T4}) D_{=k}(x_3; M_f^2) D_{=l}(x_4; M_f^2) \\
 &\int_{x_1^0}^z \frac{dz_1}{z_1} \frac{F_{i=H_1}(x_1^0; M^2)}{x_1^0} \frac{F_{j=H_2}(x_2^0; M^2)}{x_2^0} \mathcal{M}_{1j^0; k1}^{2B} \\
 &\frac{C_i}{C_{i^0}} \frac{a_{i^0i}^{(d,4)}(z_1)}{(1-z_1)_+} + \ln \frac{P_{Tm}^2}{M^2} P_{i^0i}^{(4)}(z_1) f_{i^0i}(z_1) \quad (A.8)
 \end{aligned}$$

where the variables  $x_1^0$  (resp.  $x_2^0$ ) are defined by:

$$\begin{aligned}
 x_1^0 &= \frac{p_T}{S} e^{y_3} + e^{y_4} \\
 x_2^0 &= \frac{p_T}{S} (e^{y_3} + e^{y_4})
 \end{aligned}$$

and  $p_T$  stands for  $p_{T3}$  or  $p_{T4}$ .

The finite part associated to the collinear divergence  $p_2 // p_5$  is given by:

$$\begin{aligned}
 \Gamma_{5=2} &= \int_{x_{3m}^0}^z \int_{x_{4m}^0}^z \int_{x_3^0}^z \int_{x_4^0}^z \frac{dx_3}{x_3} \frac{dx_4}{x_4} \\
 &\frac{s^{(2)}}{2} C_{ij}^B P_T (p_{T3} p_{T4}) D_{=k}(x_3; M_f^2) D_{=l}(x_4; M_f^2) \\
 &\int_{x_2^0}^z \frac{dz_2}{z_2} \frac{F_{i=H_1}(x_1^0; M^2)}{x_1^0} \frac{F_{j=H_2}(x_2^0; M^2)}{x_2^0} \mathcal{M}_{1j^0; k1}^{2B} \\
 &\frac{C_j}{C_{j^0}} \frac{a_{j^0j}^{(d,4)}(z_2)}{(1-z_2)_+} + \ln \frac{P_{Tm}^2}{M^2} P_{j^0j}^{(4)}(z_2) f_{j^0j}(z_2^0) \quad (A.9)
 \end{aligned}$$

with

$$C_{ij}^B = \frac{2}{4S^2} \frac{s^{(2)}}{C_i C_j}$$

The functions  $a_{ij}^{(d,4)}(z)$ ,  $P_{ij}^{(4)}(z)$  and  $f_{ij}(z)$  will be defined at the end of this appendix cf. equations from (A.18) to (A.21), (A.13) and (A.24).

## A.3 Pseudo cross section for the final state collinear parts

These parts contain the collinear singularities which have been absorbed into the bare fragmentation functions.

The finite part associated to the collinear divergence  $p_3 // p_5$  is given by:

$$\begin{aligned}
5=3 = & \int_{z_3}^Z \int_{y_3}^Z \int_{y_4}^Z \int_{dK_{T3}}^Z \int_{dK_{T4}}^Z \int_{x_{3m}^0}^Z \int_{x_3}^Z \int_{z_{3m}^0}^Z \int_{z_3}^Z \\
& \frac{s^{(2)}}{2} C_{ij}^B D_{=k}(x_3; M_f^2) D_{=1}(x_4^0; M_f^2) \\
& \frac{F_{i=H_1}(x_1^0; M^2)}{x_1^0} \frac{F_{j=H_2}(x_2^0; M^2)}{x_2^0} \mathcal{M}_{ij!}^{2B} k^0 \\
& \frac{a_{kk^0}^{(d,4)}(z_3)}{(1-z_3)_+} + \ln \frac{p_{T3}^2}{M_f^2} P_{kk^0}^{(4)}(z_3) d_{kk^0}(z_3) \\
& + 2 \frac{\ln(1-z_3)}{(1-z_3)} a_{kk^0}^{(4)}(z_3) + \ln(R^2) \frac{a_{kk^0}^{(4)}(z_3)}{(1-z_3)} (z_{3m} z_3)
\end{aligned} \tag{A.10}$$

whereas the finite part associated to the collinear divergence  $p_4 // p_5$  is given by:

$$\begin{aligned}
5=4 = & \int_{z_3}^Z \int_{y_3}^Z \int_{y_4}^Z \int_{dK_{T3}}^Z \int_{dK_{T4}}^Z \int_{x_{4m}^0}^Z \int_{x_4}^Z \int_{z_{4m}^0}^Z \int_{z_4}^Z \\
& \frac{s^{(2)}}{2} C_{ij}^B D_{=k}(x_3^0; M_f^2) D_{=1}(x_4; M_f^2) \\
& \frac{F_{i=H_1}(x_1^0; M^2)}{x_1^0} \frac{F_{j=H_2}(x_2^0; M^2)}{x_2^0} \mathcal{M}_{ij!}^{2B} k^0 \\
& \frac{a_{ll^0}^{(d,4)}(z_4)}{(1-z_4)_+} + \ln \frac{p_{T4}^2}{M_f^2} P_{ll^0}^{(4)}(z_4) d_{ll^0}(z_4) \\
& + 2 \frac{\ln(1-z_4)}{(1-z_4)} a_{ll^0}^{(4)}(z_4) + \ln(R^2) \frac{a_{ll^0}^{(4)}(z_4)}{(1-z_4)} (z_{4m} z_4)
\end{aligned} \tag{A.11}$$

The functions  $a_{ij}^{(4)}(z)$  and  $d_{ij}(z)$  will be also defined at the end of the appendix cf. equations from (A.14) to (A.17) and (A.25). The variables  $z_{3m}$ ,  $z_{4m}$ ,  $x_1^0$ ,  $x_2^0$ ,  $x_1^0$  and  $x_2^0$  appearing in equations (A.10) and (A.11) are given by:

$$\begin{aligned}
z_{3m} &= \frac{p_{T3}}{p_{T3} + p_{Tm}} \\
z_{4m} &= \frac{p_{T4}}{p_{T4} + p_{Tm}} \\
x_1^0 &= \frac{p_{T3} + p_{T5}}{p_{T5}} (e^{y_3} + e^{y_4}) \\
x_2^0 &= \frac{p_{T3} + p_{T5}}{p_{T5}} e^{y_3} + e^{y_4} \\
x_1^0 &= \frac{p_{T4} + p_{T5}}{p_{T5}} (e^{y_3} + e^{y_4}) \\
x_2^0 &= \frac{p_{T4} + p_{T5}}{p_{T5}} e^{y_3} + e^{y_4}
\end{aligned}$$

#### A.4 Pseudo cross section for the infrared and virtual parts

This pseudo cross section is given by:

$$\begin{aligned}
 \sigma_{ir} = & \int_{x_{3min}}^Z \int_{x_{4min}}^Z \int_{p_{T3}}^{p_T} \int_{p_{T4}}^{p_T} \\
 & \frac{s^{(2)}}{2} C_{ij}^B \frac{dx_3}{x_3} \frac{dx_4}{x_4} p_T (p_{T3} p_{T4}) \\
 & D_{=k}(x_3; M_f^2) D_{=1}(x_4; M_f^2) \frac{F_{i=H_1}(x_1^0; M^2)}{x_1^0} \frac{F_{j=H_2}(x_2^0; M^2)}{x_2^0} \\
 & \left( \ln \frac{p_T^2}{S} (b_{kk} + b_{ll}) + \ln \frac{p_{Tm}^2}{S} (b_{ii} + b_{jj}) \right) M_{ij}^{2B} \\
 & + \ln \frac{p_{Tm}^2}{S} \sum_{i < j} H_{ij}(0) \ln \frac{2p_i^0 p_j^0}{S} \\
 & \frac{1}{2} \ln \frac{p_T^2}{S} \ln \frac{p_{Tm}^2}{S} (H_{13}(0) + H_{14}(0) + H_{23}(0) + H_{24}(0) + 2H_{34}(0)) \\
 & + \frac{1}{4} \ln^2 \frac{p_T^2}{S} (H_{13}(0) + H_{14}(0) + H_{23}(0) + H_{24}(0) + 2H_{34}(0)) \\
 & \frac{1}{4} \ln^2 \frac{p_{Tm}^2}{S} (2H_{12}(0) + H_{13}(0) + H_{14}(0) + H_{23}(0) + H_{24}(0)) \\
 & + \frac{H_{34}(0)}{A_{34}(y^2)} A_{34}(y^2) + A_{34}(y^2) + F(\hat{s}; \hat{t}; \hat{u}) \tag{A.12}
 \end{aligned}$$

with  $p_T = p_{T3} = p_{T4}$ . The terms  $b_{ii}$  are defined in equations (A.22) and (A.23). In the equation (A.12),  $y^2 = (y_3 - y_4)^2$  and the function  $A(x)$  is given by:

$$\begin{aligned}
 A(x) = & \ln(2) \ln(4 \cosh^2(y^2)) + 2y^2 \sinh(2y^2) \int_0^Z \frac{\ln(\sin \theta)}{\cosh(2x) + \cos(2\theta)} d\theta \\
 & + 4 \int_0^Z \frac{\sin(2\theta)}{\cosh(2x) + \cos(2\theta)} \ln(\sin \theta) \arctan \frac{\sin \theta}{1 - \cos \theta} d\theta
 \end{aligned}$$

The function  $F$  is the finite part of the virtual term and the variables  $\hat{s}$ ,  $\hat{t}$  and  $\hat{u}$  are the Mandelstam variables of the  $2 \rightarrow 2$  processes:

$$\begin{aligned}
 \hat{s} &= (p_1^0 + p_2^0)^2 \\
 \hat{t} &= (p_1^0 - p_3^0)^2 \\
 \hat{u} &= (p_2^0 - p_3^0)^2
 \end{aligned}$$

where the 4-vectors  $p_i^0$  are the infrared limits of the 4-vectors  $p_i$ .

#### A.5 Altarelli-Parisi kernels

We will give in this appendix the expressions of the functions  $a_{ij}(z)$  and  $b_{ij}$ . These functions are defined by:

$$\begin{aligned}
P_{ij}^{(d)}(z) &= \frac{a_{ij}^{(d)}(z)}{(1-z)_+} + b_{ij}(1-z) \\
&= \frac{a_{ij}^{(4)}(z) - a_{ij}^{(d-4)}(z)}{(1-z)_+} + b_{ij}(1-z) \\
&= P_{ij}^{(4)}(z) - \frac{a_{ij}^{(d-4)}(z)}{(1-z)_+}
\end{aligned} \tag{A.13}$$

where  $P_{ij}^{(4)}$  (resp.  $P_{ij}^{(d)}$ ) are the Altarelli-Parisi Kernels in four (resp.  $d$ ) dimensions. So the expressions for the functions  $a_{ij}^{(4)}(z)$ ,  $a_{ij}^{(d-4)}(z)$  and  $b_{ij}$  are given by:

$$a_{gg}^{(4)}(z) = 2N_c z + \frac{(1-z)^2}{z} + z(1-z)^2 \tag{A.14}$$

$$a_{qq}^{(4)}(z) = C_F(1+z^2) \tag{A.15}$$

$$a_{gq}^{(4)}(z) = C_F \frac{1+(1-z)^2}{z}(1-z) \tag{A.16}$$

$$a_{qq}^{(4)}(z) = T_F(z^2 + (1-z)^2)(1-z) \tag{A.17}$$

where  $N_c$  is the number of colors,  $C_F = (N_c^2 - 1)/(2N_c)$  and  $T_F = 1/2$ . The extra part needed to get the functions  $a$  in  $d$  dimensions ( $a_{ij}^{(d)}(z) = a_{ij}^{(4)}(z) - a_{ij}^{(d-4)}(z)$ ) is given by:

$$a_{gg}^{(d-4)}(z) = 0 \tag{A.18}$$

$$a_{qq}^{(d-4)}(z) = C_F(1-z)^2 \tag{A.19}$$

$$a_{gq}^{(d-4)}(z) = C_F z(1-z) \tag{A.20}$$

$$a_{qq}^{(d-4)}(z) = 2T_F z(1-z)^2 \tag{A.21}$$

The coefficients  $b_{ij}$  read:

$$b_{gg} = \frac{(11N_c - 2N_c F)}{6} \tag{A.22}$$

$$b_{qq} = \frac{3}{2} C_F \tag{A.23}$$

The function  $f_{ij}(x)$  and  $d_{ij}(z)$  define the factorisation scheme for respectively initial state and final state collinear singularities. In the  $\overline{MS}$  scheme, we have:

$$f_{ij}(z) = 0 \tag{A.24}$$

$$d_{ij}(z) = 0 \tag{A.25}$$

## B Cancellation of the $p_{Tm}$ and $R_{th}$ dependences

In this appendix, we give further details on the cancellation of the  $p_{Tm}$  and  $R_{th}$  dependences in observables calculated according to the method used in this article.

In the conical parts II a and II b, the d-dimensional integration over particle 5 in  $C_i$ ,  $i = 3;4$ , reads schematically:

$$i = \int_{P_{Tm}Z}^{Z_{P_{T5max}}} dp_{T5} p_{T5}^{1/2} \int_{C_i} d_{i5} dy_5 \sin^2_{i5} \frac{F(p_{T5}; i_5; Y_5)}{\cosh(Y_i - Y_5) \cos_{i5}} \quad (B.1)$$

The term generating the final state collinear pole ( $p_5/p_i$ ) has been explicitly written, and the remaining quantity  $F(p_{T5}; i_5; Y_5)$  is a regular function. In the parts II a and II b, the same subtraction method as in [15] is used, and the following contribution is added and subtracted:

$$i^{sub} = \int_{P_{Tm}}^{Z_{P_{T5max}}} dp_{T5} p_{T5}^{1/2} \int_{C_i} d_{i5} dy_5 \int_{i5}^2 \frac{2F(p_{T5}; 0; Y_i)}{(Y_i - Y_5)^2 + \frac{2}{i5}} \quad (B.2)$$

In the cylindrical part I, the finite terms produced by the integration over particle 5 are approximated: all the terms depending logarithmically on  $p_{Tm}$  are kept, whereas terms proportional to powers of  $p_{Tm}$  are neglected. Notice that this differs from the subtraction method implemented in the cylinder in [15], which kept the exact  $p_{Tm}$  dependence.

In summary, the present method is an admixture of the phase space slicing and subtraction methods, at variance with what has been done in [15]. It ensures the exact cancellation of the unphysical parameter  $R_{th}$  dependence between part II c and parts II a, II b whereas only an approximated cancellation of the unphysical parameter  $p_{Tm}$  dependence between parts II c, II a and II b and part I occurs.

We checked carefully that the dependences on the unphysical parameters drop out. This point is illustrated by the  $p_{Tm}$  dependence (at fixed  $R_{th} = 0.1$ ) and the  $R_{th}$  dependence (at fixed  $p_{Tm} = 0.1$  GeV), of the higher order (HO) part of integrated cross section (the lowest order (LO) part being independent of these parameters)

$$HO = \int_{m_{min}}^{Z_{m_{max}}} dm \frac{d^{HO}}{dm}$$

shown on Figs. 15 and 16. We display separately the qq and qg initiated contributions to the "direct" on Fig. 15, and the "one-" and "two fragmentation" mechanisms, on Fig. 16. To be definite, the integration bounds are taken to be  $m_{min} = 80$  GeV,  $m_{max} = 1500$  GeV, the cuts  $p_{T3}, p_{T4} = 25$  GeV,  $|y_{3,4}| \leq 2.5$  are applied, and the MRST2 set of parton distribution functions with the scale choice  $M = M_f = m = 2$  are used; let us emphasize however that the pattern obtained does not depend on these details.

The quantity  $HO$  does not depend on  $R_{th}$  and, in principle, it becomes independent of  $p_{Tm}$  at small enough  $p_{Tm}$ . To show these features more clearly, the observable displayed is the ratio  $R_m$  defined as follows:

$$R_m = \frac{1}{A} \int_{m_{min}}^{Z_{m_{max}}} dm \frac{d^{HO}}{dm} \quad (B.3)$$

The integrated cross section is normalized to be asymptotically 1 in order to show the size of the relative error bars. However taking the denominator  $A$  equal to the calculated  $HO$  for the



- [1] A. Djouadi, D. Graudenz, M. Spira and P. Zerwas, Nucl. Phys. B 453 (1995) 17.
- [2] V. DelDuca, W. B. Kilgore and F. Maltoni, hep-ph/9910253.
- [3] D. de Florian and Z. Kunszt, Phys. Lett. 460B (1999) 184;  
C. Balazs, P. Nadolsky, C. Schmidt and C. P. Yuan, hep-ph/9905551.
- [4] V. A. Smirnov, Phys. Lett. 460B (1999) 397;  
J. B. Tausk, hep-ph/9909506.
- [5] P. Chiappetta, R. Fergani and J.-P. Guillet, Z. Phys. C 69 (1996) 443.
- [6] M. A. Furman Nucl. Phys. B 197 (1982) 413;  
W. T. Giele and E. W. N. Glover, Phys. Rev. D 46 (1992) 1980;  
W. T. Giele, E. W. N. Glover and D. Kosower, Nucl. Phys. B 403 (1993) 633.
- [7] R. K. Ellis, D. A. Ross and A. E. Terrano, Nucl. Phys. B 187 (1981) 421;  
S. Frixione, Z. Kunszt and A. Signer, Nucl. Phys. B 467 (1996) 399;  
S. Catani and M. H. Seymour, Nucl. Phys. B 485 (1997) 291.
- [8] S. Kawabata, Comp. Phys. Comm. 88 (1995) 309.
- [9] R. Brun, O. Couet, G. E. Vandoni and P. Zabarini, Comp. Phys. Comm. 57 (1989) 432;  
PAW, Physics Analysis Workstation, CERN Program Library Q 121  
(<http://www.info.cern.ch/asd/paw/index.html>).
- [20] H.-U. Bengtsson and T. Sjöstrand, Comp. Phys. Comm. 46 (1987) 43;  
T. Sjöstrand, Comp. Phys. Comm. 82 (1994) 74;  
T. Sjöstrand, LU TP 95-20, hep-ph/9508391.
- [21] G. Marchesini and B. R. Webber, Nucl. Phys. B 310 (1988) 461;  
G. Marchesini, B. R. Webber, G. Abbiendi, I. G. Knowles, M. H. Seymour and L. Stanco, hep-ph/9607393.
- [22] S. Frixione, Phys. Lett. 429B (1998) 369.
- [23] H. Baer, J. Ohnemus and J. F. Owens, Phys. Rev. D 42 (1990) 61.
- [24] P. Aurenche, R. Baier and M. Fontannaz, Phys. Rev. D 42 (1990) 1440.
- [25] E. L. Berger and J. Qiu, Phys. Rev. D 44 (1991) 2002.
- [26] L. E. Gordon and W. Vogelsang, Phys. Rev. D 50 (1994) 1901.
- [27] S. Catani, M. Fontannaz and E. Pilon, work in preparation.
- [28] Z. Kunszt and Z. Troscanyi, Nucl. Phys. B 394 (1993) 139.
- [29] E. L. Berger, X. F. Guo and J. W. Qiu, Phys. Rev. D 54 (1996) 5470.
- [30] S. Catani, M. Fontannaz and E. Pilon, Phys. Rev. D 58 (1998) 094025.
- [31] E. W. N. Glover and A. G. Morgan, Z. Phys. C 62 (1994) 311.

- [32] P. Aurenche, R. Baier, M. Fontannaz, J. Owens and M. W erlen, *Phys. Rev. D* 39 (1989) 3275.
- [33] P. Aurenche, R. Baier, M. Fontannaz, M. N. Kienzle-Focacci and M. W erlen, *Phys. Lett.* 233B (1989) 517.
- [34] P. J. Sutton, A. D. Martin, R. G. Roberts and W. J. Stirling, *Phys. Rev. D* 45 (1992) 2349.
- [35] M. Glück, E. Reya and A. Vogt, *Z. Phys. C* 53 (1992) 651.
- [36] B. Abbott et al., *Phys. Rev. D* 58 (1998) 092003
- [37] A. D. Martin, R. G. Roberts, W. J. Stirling and R. S. Thome, *hep-ph/9907231*.
- [38] J. Womersley, private communication.
- [39] J. F. Owens, private discussion.
- [40] CMS technical proposal CERN/LHCC 94-38 (p 179);  
 ATLAS technical proposal CERN/LHCC 94-43;  
 V. Tisserand for the ATLAS collaboration, in *Proc. 6th Int. Conf. on Calorimetry in High Energy Physics (ICCHEP 96)*, ed. by A. Antonelli, S. Bianco, A. Calcaterra, F. L. Fabbri, (Frascati physics series; 6) p 475.
- [41] Y. Dokshitzer, D. Dyakonov and S. Troyan, *Phys. Rep.* 58 (1980) 269;  
 A. Basseto, M. Ciafaloni and G. Marchesini, *Phys. Rep.* 100 (1983) 201 and references therein;  
 see also [43].
- [42] C. Balazs, private communication.
- [43] J. Collins and D. Soper, *Nucl. Phys. B* 193 (1981) 381;  
 J. Collins and D. Soper, *Nucl. Phys. B* 197 (1982) 446;  
 J. Collins, D. Soper and G. Sterman, *Nucl. Phys. B* 250 (1985) 199.
- [44] R. Bonciani, S. Catani, M. Mangano and P. Nason, *Nucl. Phys. B* 529 (1998) 424;  
 N. Kidonakis, G. Oderda and G. Sterman, *Nucl. Phys. B* 531 (1998) 365.
- [45] S. Catani and B. Webber, *JHEP* 9710:005 (1997).
- [46] R. K. Ellis and J. C. Sexton, *Nucl. Phys. B* 269 (1986) 445.

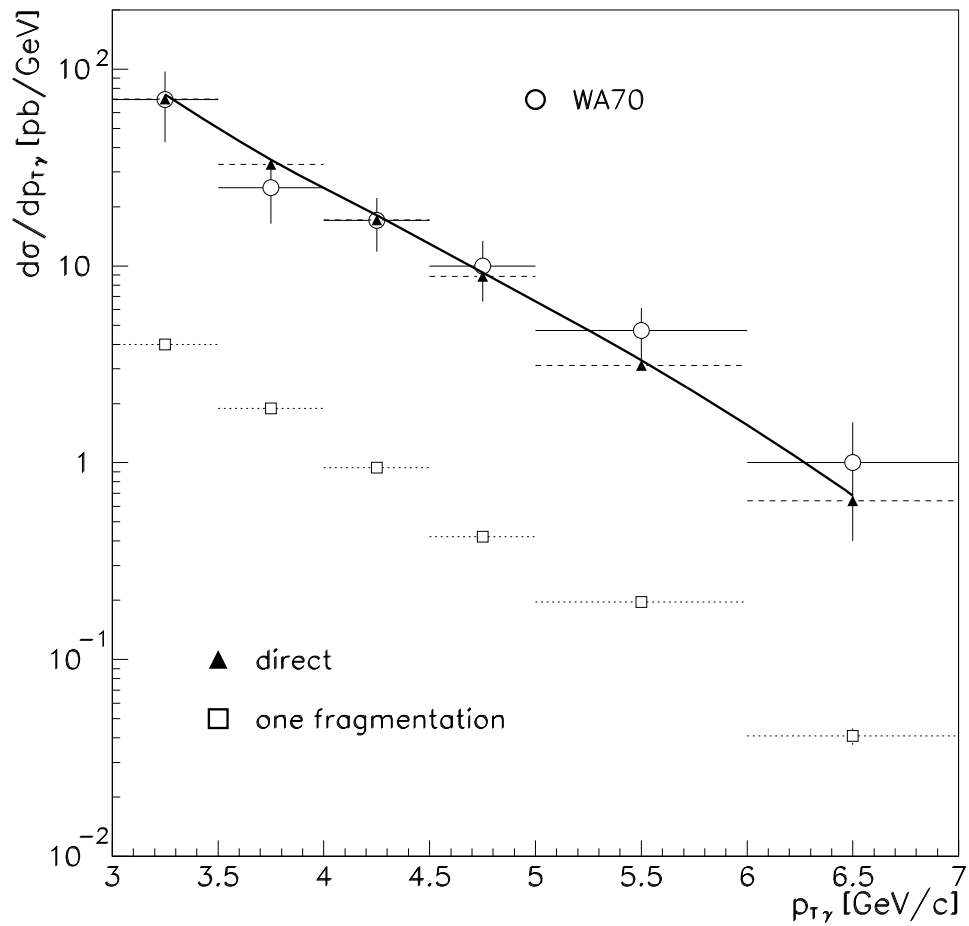


Figure 1: Diphoton differential cross section  $d\sigma/dp_T$  vs.  $p_T$ , the transverse energy of each photon, in  $p$ -proton collisions at  $\sqrt{s} = 22.9$  GeV. Data points from the WA70 collaboration [1]. The solid line is the full contribution with scales  $M = M_f = 0.275(p_T(1) + p_T(2))$ .

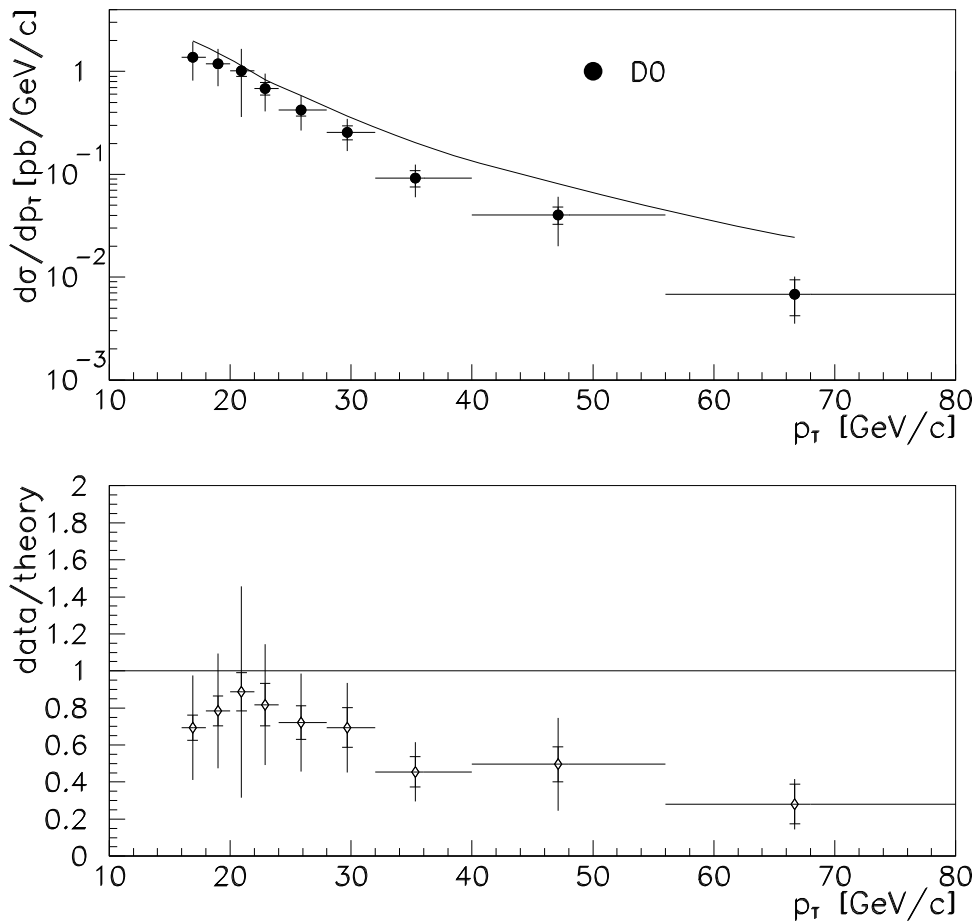


Figure 2:  $D_0$  photon differential cross section  $d\sigma/dp_T$  vs  $p_T$ , the transverse energy of each photon, at Tevatron,  $\sqrt{S} = 1.8$  TeV. Preliminary data points (statistical errors and systematics in quadrature) from the D0 collaboration [6] are compared to the theoretical predictions: the full NLO prediction is shown as the solid line. The ratio data/(full NLO theory) is shown below.

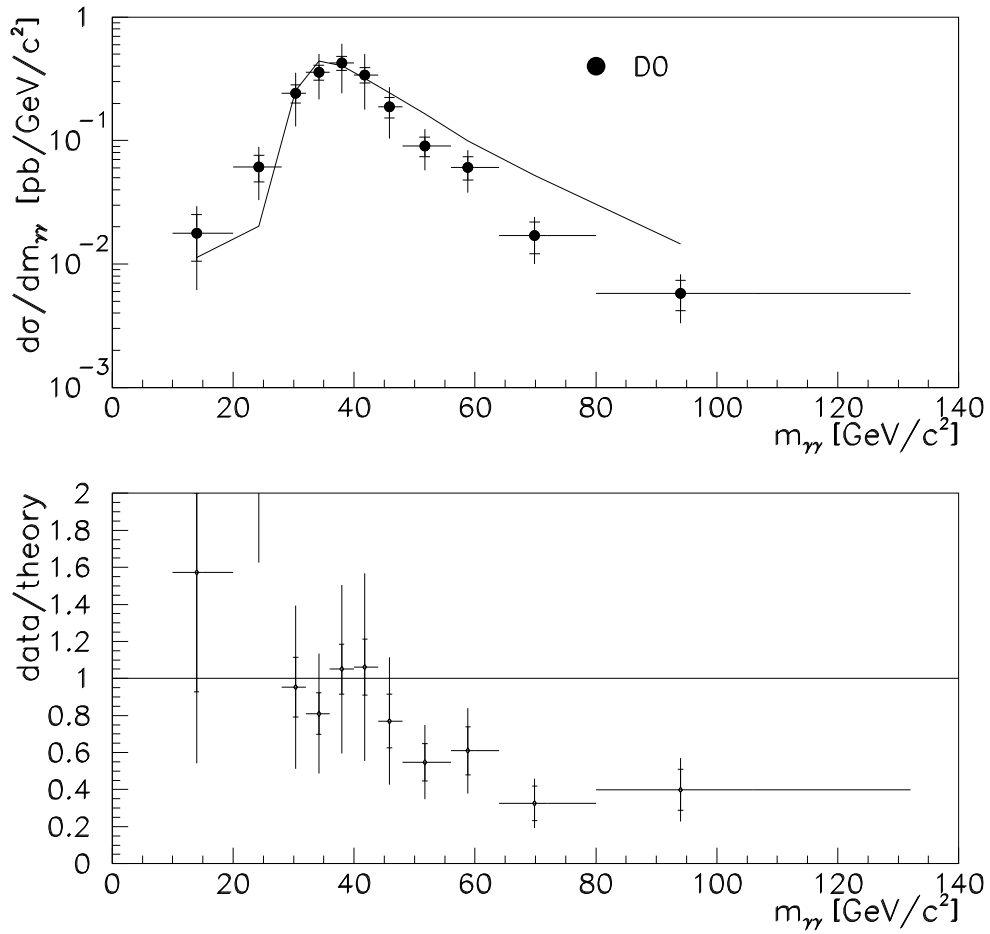


Figure 3:  $D_0$  photon differential cross section  $d\sigma/dm_{\gamma\gamma}$  vs.  $m_{\gamma\gamma}$ , the mass of the photon pair, at Tevatron,  $\sqrt{s} = 1.8$  TeV. Preliminary data points (statistical errors and systematics in quadrature) from the  $D_0$  collaboration [6] are compared to the theoretical predictions: the full NLO prediction is shown as the solid line.

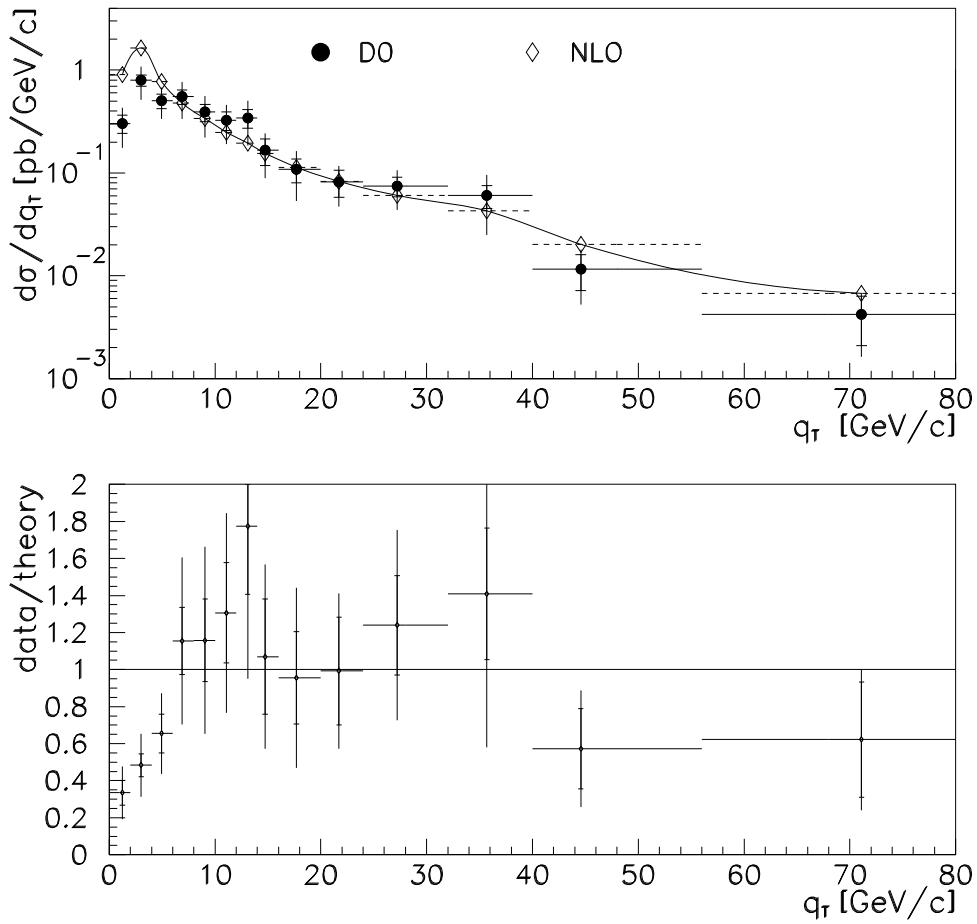


Figure 4: Diphoton differential cross section  $d\sigma/dq_T$  vs.  $q_T$ , the transverse momentum of the photon pair, at Tevatron,  $\sqrt{s} = 1.8$  TeV. Preliminary data points (statistical errors and systematics in quadrature) from the D0 collaboration [6] are compared to the theoretical predictions: the full NLO prediction is shown as the solid line

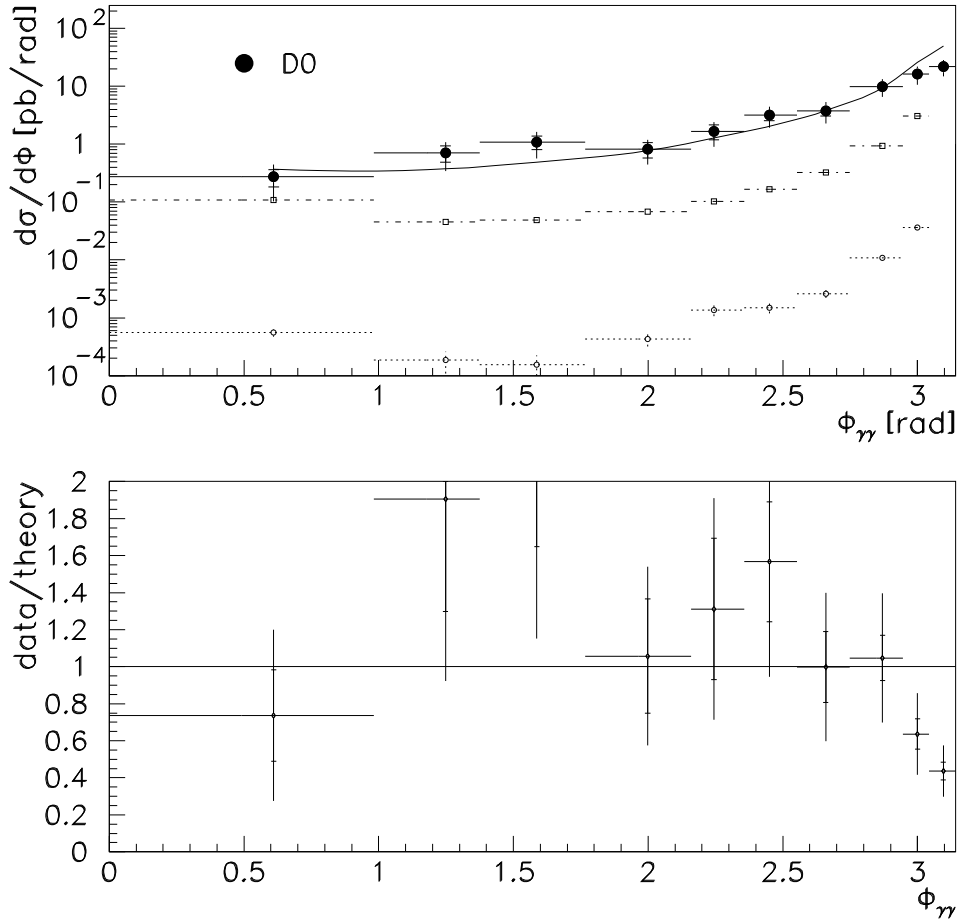


Figure 5: Diphoton differential cross section  $d\sigma/d\phi$  vs.  $\phi_{\gamma\gamma}$ , the azimuthal angle between the two photons, at Tevatron,  $\sqrt{s} = 1.8$  TeV. Preliminary data points (statistical errors and systematics in quadrature) from the D0 collaboration [6] are compared to the theoretical predictions: the full NLO prediction is shown as the solid line while open squares (open circles) represent the single (double) fragmentation contribution.

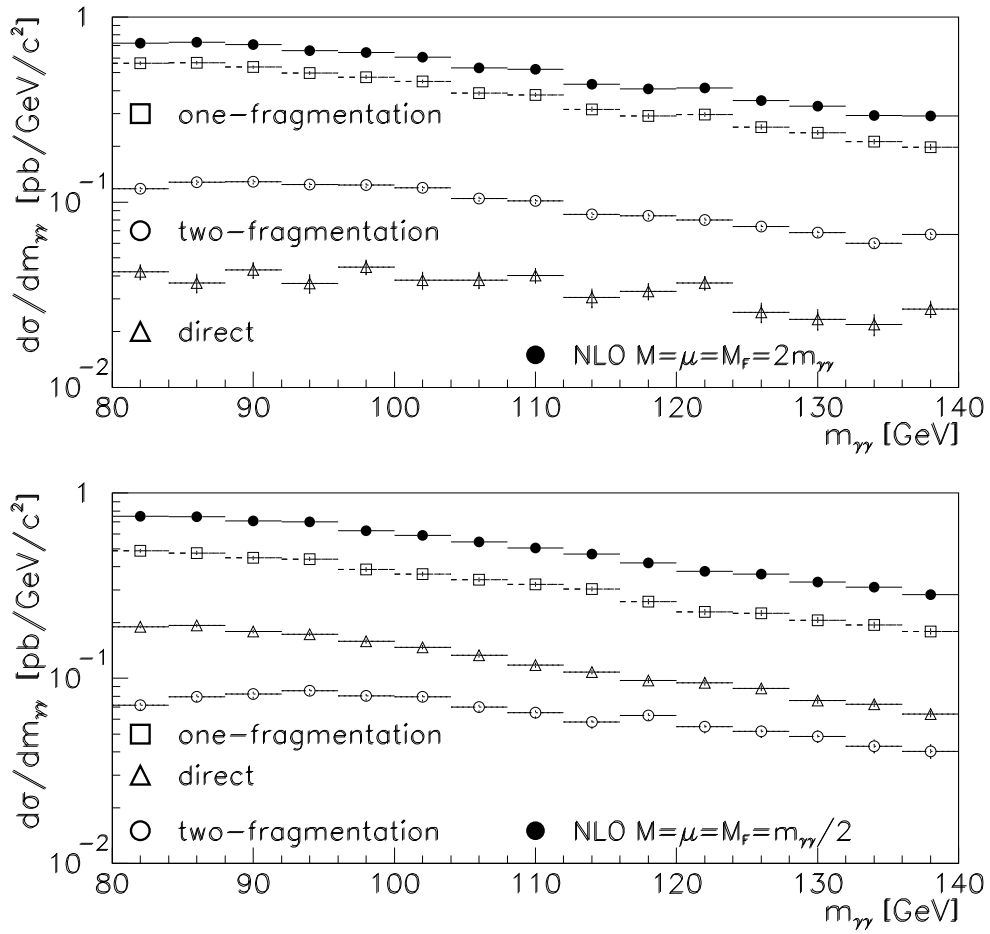


Figure 6: Splitting of the diphoton differential cross section  $d\sigma/dm_{\gamma\gamma}$  at LHC,  $\sqrt{s} = 14 \text{ TeV}$  without isolation, into the "direct", "one fragmentation" and "two fragmentation" components, shown for two different choices of scales. The following kinematic cuts are applied:  $p_T(1) < 40 \text{ GeV}$ ,  $p_T(2) < 25 \text{ GeV}$ ,  $|\Delta\eta(1,2)| < 2.5$ .

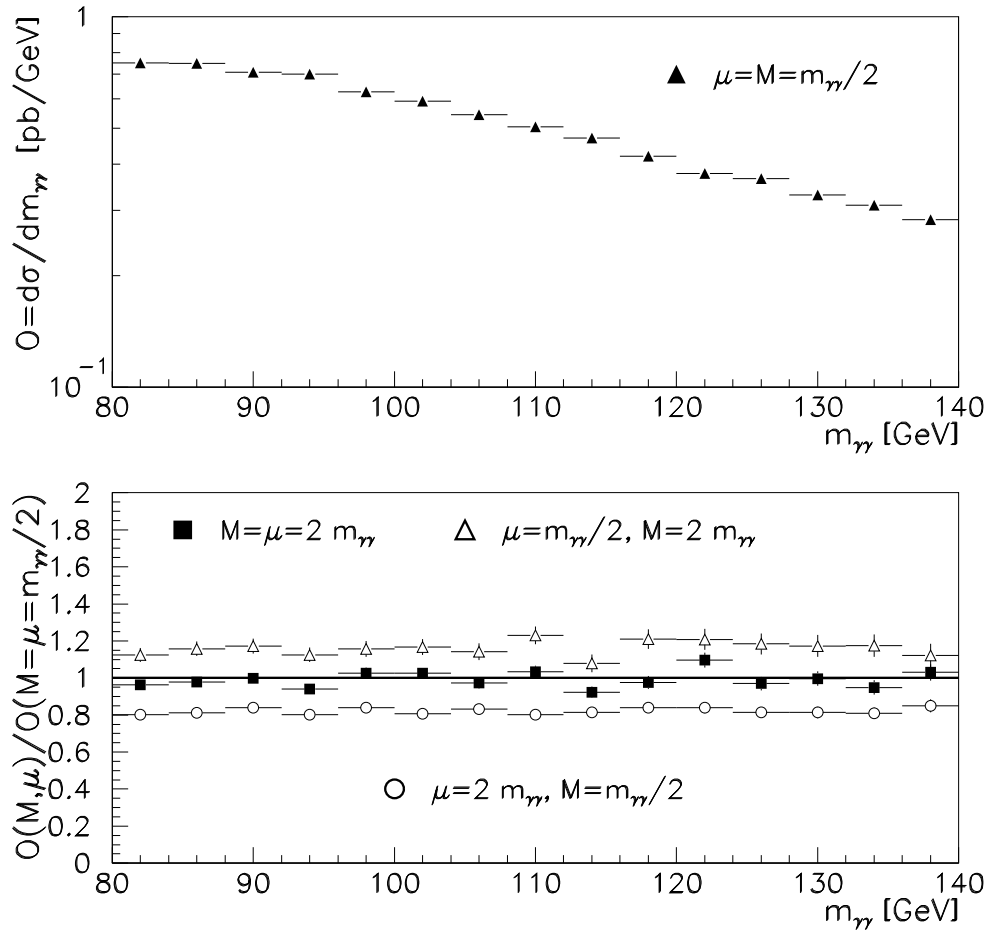


Figure 7: Diphoton differential cross section  $d\sigma/dm_{\gamma\gamma}$  vs.  $m_{\gamma\gamma}$ , the invariant mass of photon pairs, at LHC,  $\sqrt{s} = 14$  TeV without isolation. The following kinematic cuts are applied:  $p_T(1) \geq 40$  GeV,  $p_T(2) \geq 25$  GeV,  $|\eta(1,2)| \leq 2.5$ . The scale dependence is shown on the bottom plot.  $M = M_f$  is understood.

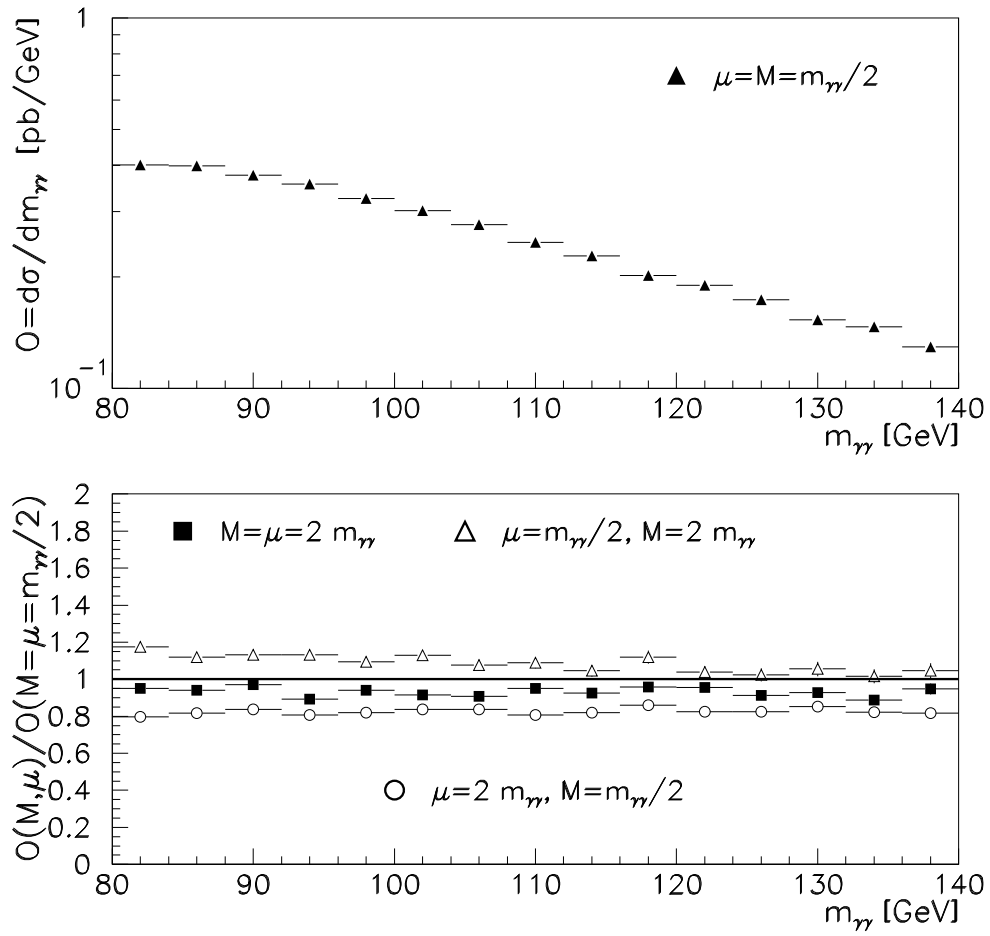


Figure 8: Diphoton differential cross section  $d\sigma/dm_{\gamma\gamma}$  vs.  $m_{\gamma\gamma}$  at LHC,  $\sqrt{s} = 14$  TeV, with isolation criterion  $E_{Tmax} = 5$  GeV in  $R = 0.4$ . Same kinematic cuts as in Fig. 7. The scale dependence is shown on the bottom plot.  $M = M_f$  is understood.

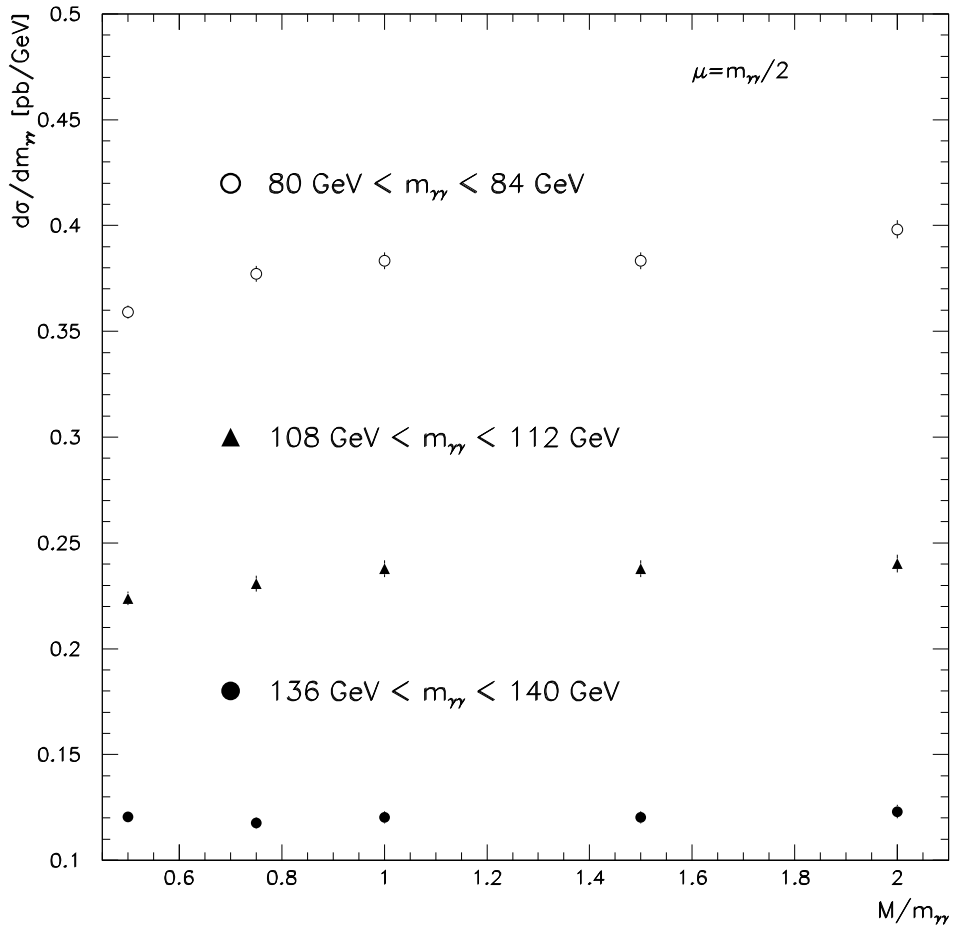


Figure 9:  $M$  dependence of the "direct+box" contribution to  $d\sigma/dm_{\gamma\gamma}$  in several  $m_{\gamma\gamma}$  bins at LHC,  $\sqrt{s} = 14$  TeV, with isolation criterion  $E_{Tmax} = 5$  GeV in  $R = 0.4$ . Same kinematic cuts as in Fig. 7.  $\mu$  is chosen to be  $m_{\gamma\gamma}/2$ , while  $M$  is varied between  $m_{\gamma\gamma}/2$  and  $2m_{\gamma\gamma}$ .

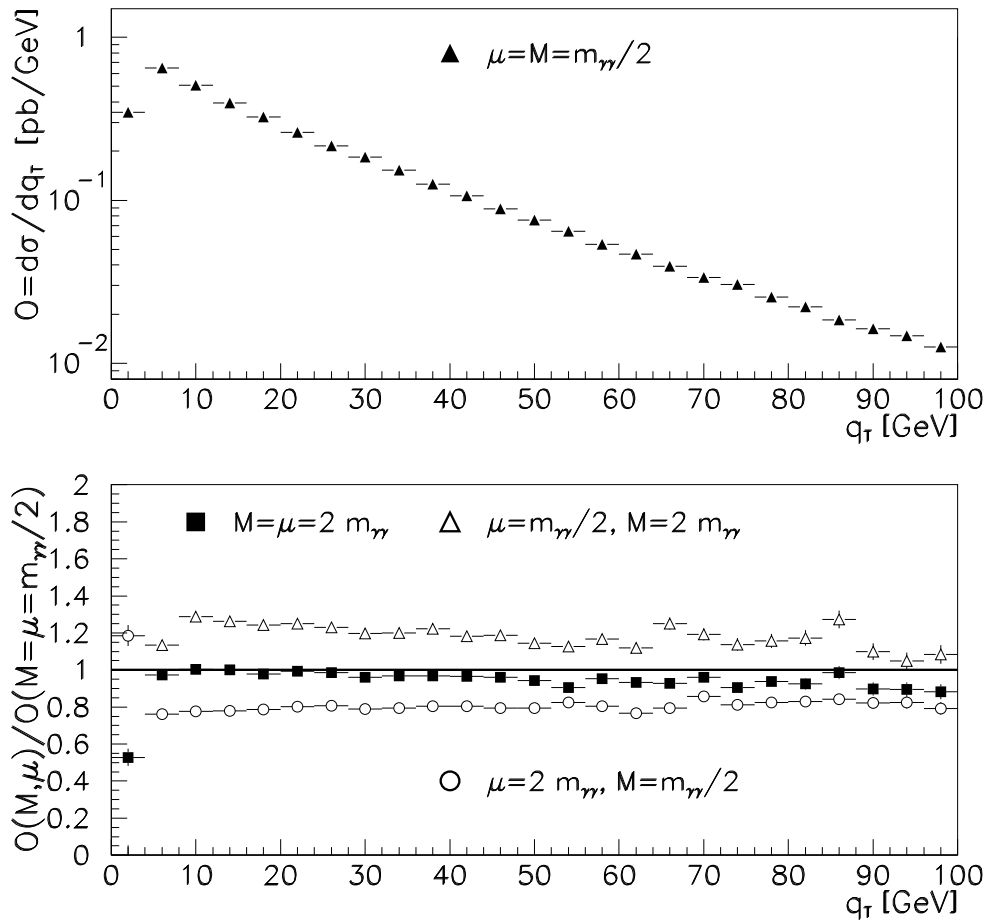


Figure 10: Diphoton differential cross section  $d = dq_T$  at LHC,  $\sqrt{s} = 14$  TeV, with isolation criterion  $E_{T \max} = 5$  GeV in  $R = 0.4$ . The following kinematic cuts are applied:  $p_T(1) \geq 40$  GeV,  $p_T(2) \geq 25$  GeV,  $|\eta(1,2)| \leq 2.5$ , and  $80 \text{ GeV} \leq m \leq 140 \text{ GeV}$ . The scale dependence is shown on the bottom plot.  $M = M_f$  is understood.

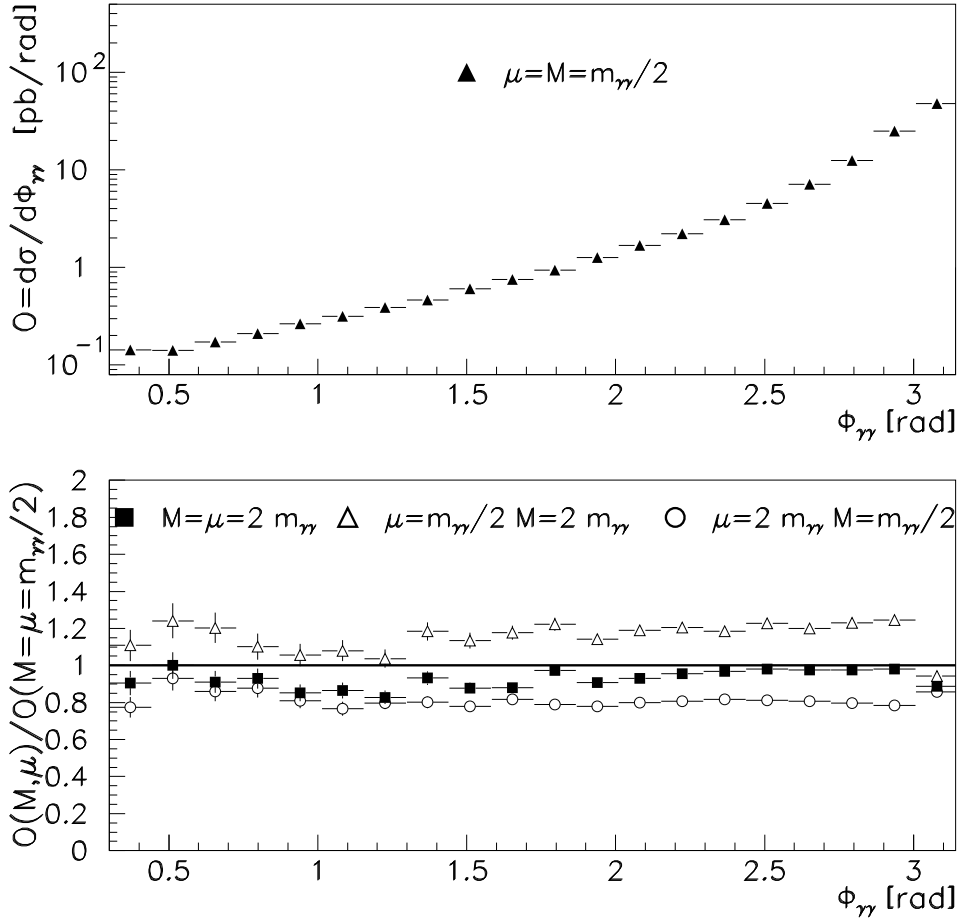


Figure 11: Diphoton differential cross section  $O = d\sigma/d\phi_{\gamma\gamma}$  vs.  $\phi_{\gamma\gamma}$ , the azimuthal angle between the two photons, at LHC,  $\sqrt{s} = 14$  TeV, with isolation criterion  $E_{Tmax} = 15$  GeV in  $R = 0.4$ . Same kinematic cuts as in Fig. 10. The scale dependence is shown on the bottom plot.  $M = M_f$  is understood.

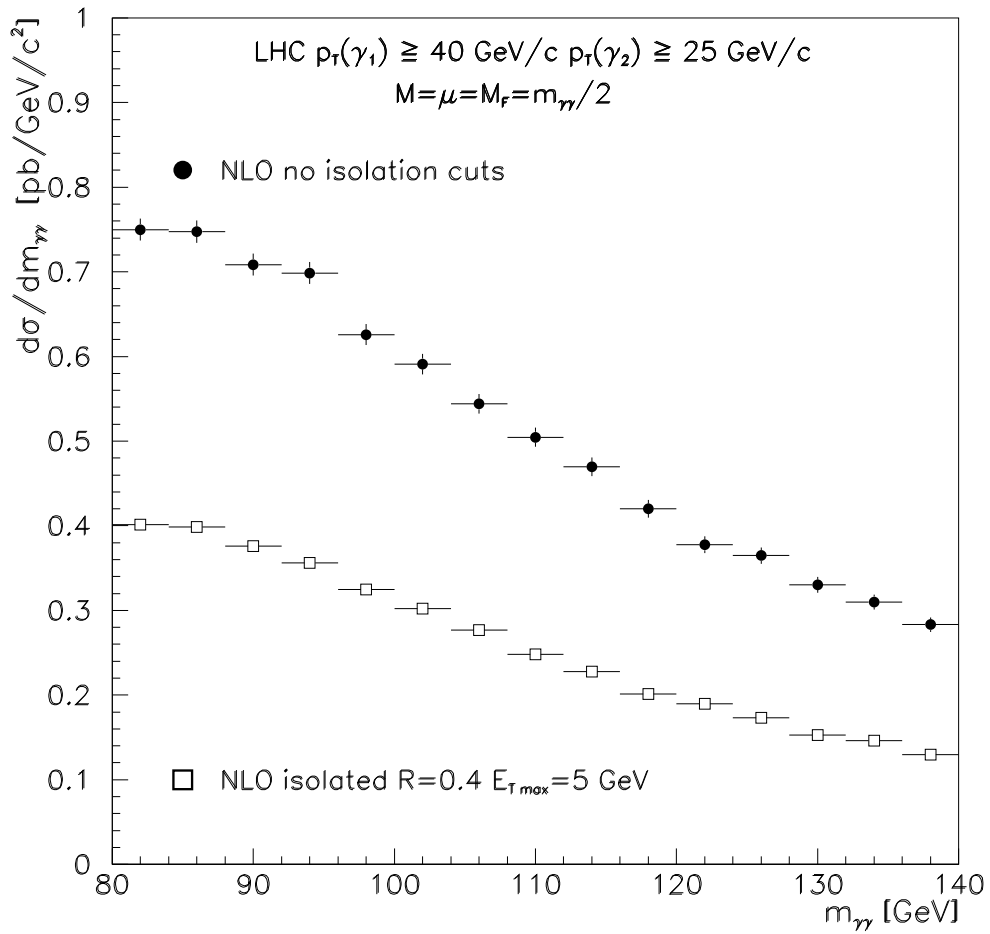


Figure 12: Diphoton differential cross section  $d\sigma/dm_{\gamma\gamma}$  vs.  $m_{\gamma\gamma}$  at LHC,  $\sqrt{s} = 14 \text{ TeV}$ , without and with isolation criterion  $E_{Tmax} = 5 \text{ GeV}$  in  $R = 0.4$ . Same kinematic cuts as in Fig. 7. The scale choice is  $M = M_f = m_{\gamma\gamma} = 2$ .

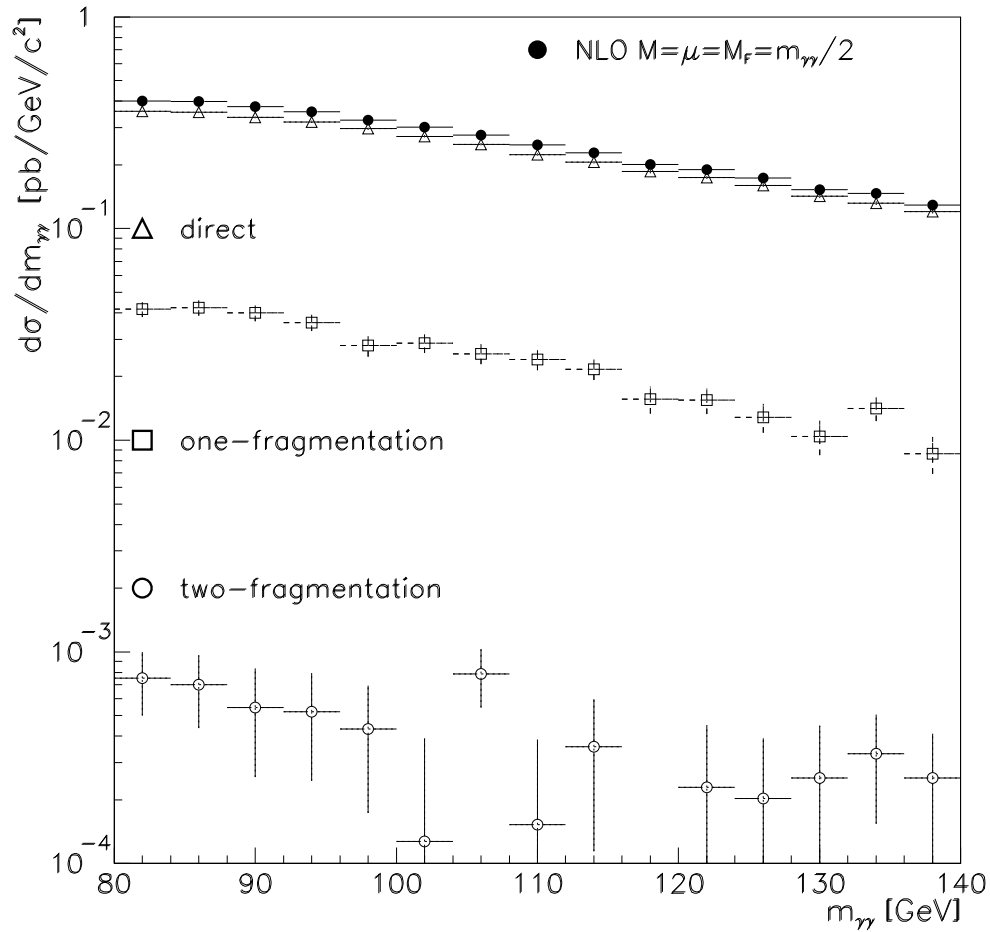


Figure 13: Splitting of the diphoton differential cross section  $d\sigma/dm_{\gamma\gamma}$  at LHC,  $\sqrt{s} = 14$  TeV with isolation criterion  $E_{Tmax} = 5$  GeV in  $R = 0.4$ , into the "direct", "one fragmentation" and "two fragmentation" components, shown for the scale choice  $\mu = M = M_f = m_{\gamma\gamma}/2$ . The following kinematic cuts are applied:  $p_T(\gamma_1) \geq 40$  GeV,  $p_T(\gamma_2) \geq 25$  GeV,  $|\Delta\eta(\gamma_1, \gamma_2)| \geq 2.5$ .

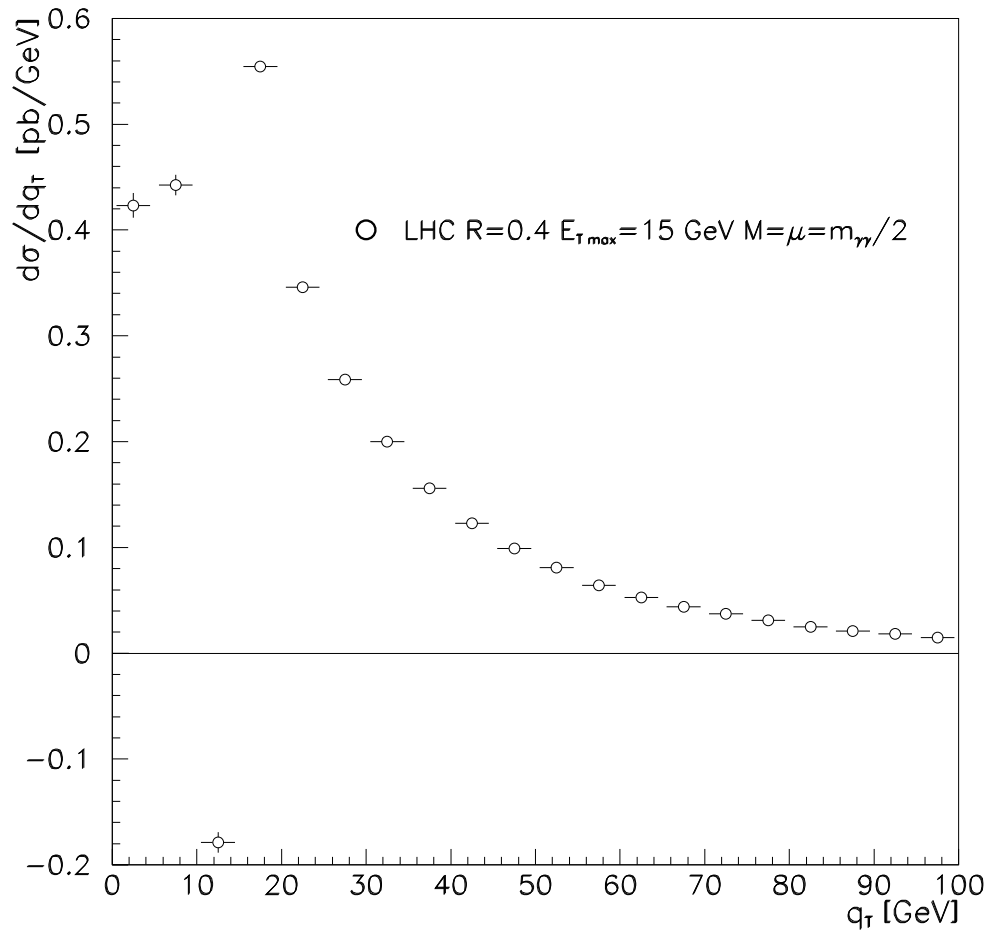


Figure 14: Diphoton differential cross section  $d\sigma/dq_T$  at LHC,  $\sqrt{s} = 14$  TeV, with isolation criterion  $E_{T,max} = 15$  GeV in  $R = 0.4$ . Same kinematic cuts as in Fig. 7.

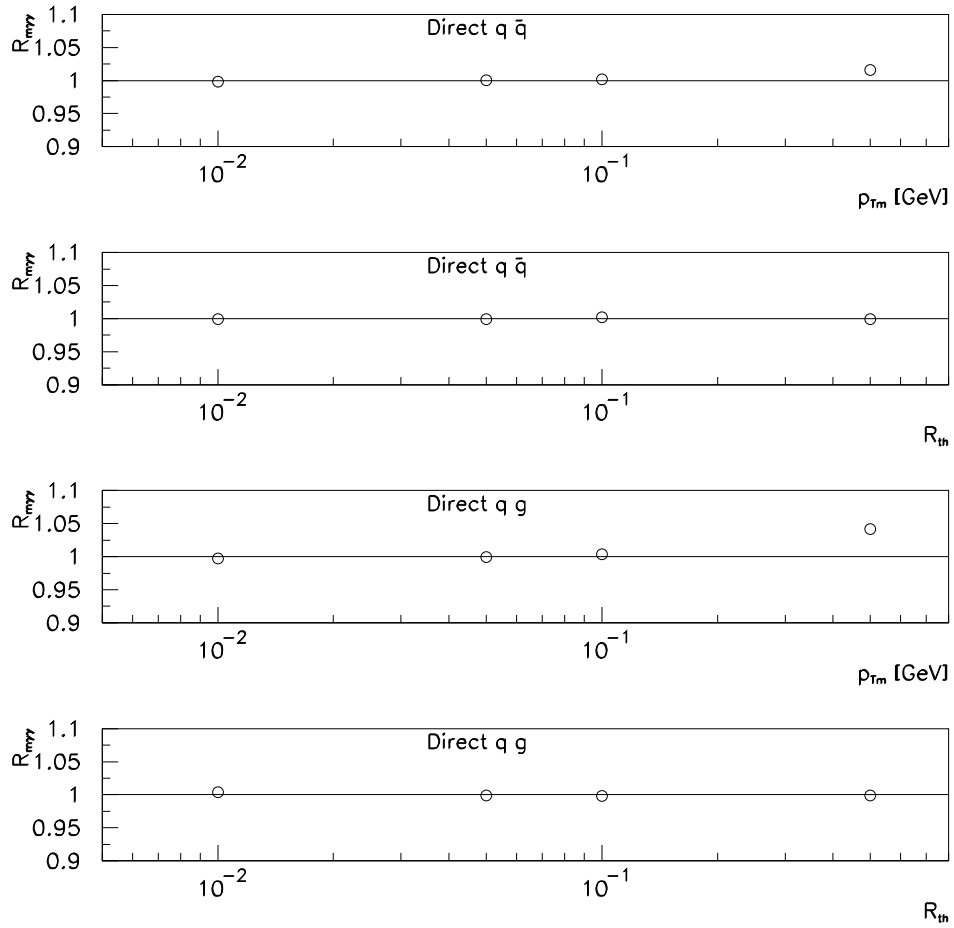


Figure 15: Dependence of the ratio  $R_m$  (see equation (B.3)) over the phase space slicing parameters  $R_{th}$  and  $p_{Tm}$  for the "direct" contribution.

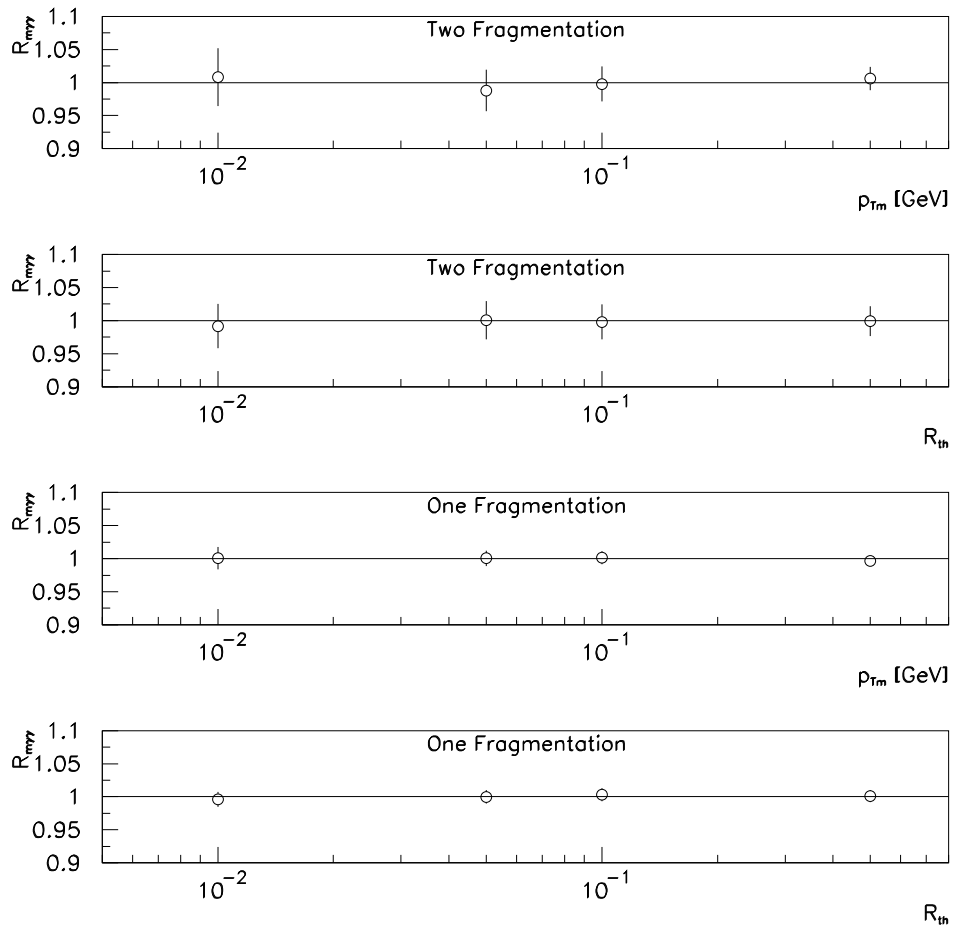


Figure 16: Dependence of the ratio  $R_m$  (see equation (B.3)) over the phase space slicing parameters  $R_{th}$  and  $p_{Tm}$  for the "one" and "two fragmentation" contributions.